Kinetic and structural insight into a role of the re-face Tyr328 residue of the homodimer type ferredoxin-NADP+ oxidoreductase from Rhodopseudomonas palustris in the reaction with NADP+/NADPH

doi: 10.1016/j.bbabio.2019.148140

Kinetic and structural insight into a role of the *re*-face Tyr328 residue of the homodimer type ferredoxin-NADP$^+$ oxidoreductase from *Rhodopseudomonas palustris* in the reaction with NADP$^+$/NADPH

Daisuke Seo[a#*], Norifumi Muraki[b,c,d#], Genji Kurisu[d,e*]

[a]Division of Material Science, Graduate School of Natural Science and Technology, Kanazawa University. Kakuma, Kanazawa, Ishikawa 920-1192, Japan
[b]Department of Creative Research, Exploratory Research Center on Life and Living Systems (ExCELLS), National Institutes of Natural Sciences (NINS), 5-1 Higashiyama, Myodaiji-cho, Okazaki 444-8787, Japan
[c]Institute for Molecular Science, National Institutes of Natural Sciences, 5-1 Higashiyama, Myodaiji-cho, Okazaki 444-8787, Japan
[d]Department of Life Sciences, University of Tokyo, Komaba, Meguro-ku, Tokyo 153-8902, Japan
[e]Institute for Protein Research, Osaka University, Suita, Osaka 565-0871, Japan

#: contributed equally

*To whom correspondence should be addressed:

Genji Kurisu
Institute for Protein Research, Osaka University, Suita, Osaka 565-0871, Japan
Email: gkurisu@protein.osaka-u.ac.jp

Daisuke Seo
Division of Material Science, Graduate School of Natural Science and Technology, Kanazawa University, Kakuma, Kanazawa, Ishikawa 920-1192, Japan
Tel: +81-76-264-5683, Fax: +81-76-264-5742
Email: dseo@se.kanazawa-u.ac.jp

Keywords
ferredoxin; ferredoxin-NADP$^+$ oxidoreductase; stopped-flow spectrophotometry; purple non-sulfur bacteria; charge transfer complex

Abbreviations

A, absorbance; *Bs*, *Bacillus subtilis*; *Ct*, *Chlorobaculum tepidum*; CT, charge transfer; CTC, charge transfer complex; *Ec*, *Escherichia coli*; FAD, flavin adenine dinucleotide; Fd, ferredoxin; FNR, ferredoxin-NAD(P)$^+$ oxidoreductase; G6P, glucose-6-phosphate; G6PDH, glucose-6-phosphate dehydrogenase; HEPES, 4-(2-hydroxyethyl)-1-piperazineethanesulfonic acid; K_d, dissociation constant; K_M, Michaelis constant; PdR, putidaredoxin reductase; SDS-PAGE, sodium dodecyl sulfate poly acrylamide gel electrophoresis; Tris, tris(hydroxymethyl)aminomethane; TrxR, bacterial NADPH-thioredoxin reductase; Suffixes: ox, oxidized; red, reduced; WT, wild type.

Author contributions

DS and GK designed the study. DS prepared the protein samples and performed the spectroscopic measurements and kinetic analysis. NM and GK performed the crystallization and crystal structure analysis. DS, NM, and GK wrote the paper.

Conflict of interest

The authors of the manuscript "Kinetic and structural insight into a role of the *re*-face Tyr328 residue of the homodimer type ferredoxin-NADP$^+$ oxidoreductase from *Rhodopseudomonas palstris* in the reaction with NADP$^+$/NADPH" have no conflict of interest.

Abstract

Among the thioredoxin reductase-type ferredoxin-NAD(P)$^+$ oxidoreductase (FNR) family, FNR from photosynthetic purple non-sulfur bacterium *Rhodopseudomonas palustris* (*Rp*FNR) is distinctive because the predicted residue on the *re*-face of the isoalloxazine ring portion of the FAD prosthetic group is a tyrosine. Here, we report the crystal structure of wild type *Rp*FNR and kinetic analyses of the reaction of wild type, and Y328F, Y328H and Y328S mutants with NADP$^+$/NADPH using steady state and pre-steady state kinetic approaches.

The obtained crystal structure of wild type *Rp*FNR confirmed the presence of Tyr328 on the *re*-face of the isoalloxazine ring of the FAD prosthetic group through the unique hydrogen bonding of its hydroxyl group. In the steady state assays, the substitution results in the decrease of K_d for NADP$^+$ and K_M for NADPH in the diaphorase assay; however, the k_{cat} values also decreased significantly. In the stopped-flow spectrophotometry, mixing oxidized *Rp*FNRs with NADPH and reduced *Rp*FNRs with NADP$^+$ resulted in rapid charge transfer complex formation followed by hydride transfer. The observed rate constants for the hydride transfer in both directions were comparable (>400 s^{-1}). The substitution did not drastically affect the rate of hydride transfer, but substantially slowed down the subsequent release and re-association of NADP$^+$/NADPH in both directions. The obtained results suggest that Tyr328 stabilizes the stacking of C-terminal residues on the isoalloxazine ring portion of

the FAD prosthetic group, which impedes the access of $NADP^+$/NADPH on the isoalloxazine ring portions, in turn, enhancing the release of the $NADP^+$/NADPH and/or reaction with electron transfer proteins.

1. Introduction

Purple non-sulfur bacterium *Rhodopseudomonas palustris* is a metabolically versatile bacterium. The bacterium can grow photoautotrophically using H_2 and CO_2 as an electron donor and a carbon source, respectively, as well as heterotrophically with organic compounds [1, 2]. Under both aerobic and anaerobic growth conditions, the bacterium metabolizes various organic compounds including aromatic compounds derived from plant degradation as a carbon source [3–5]. The bacterium is also known to perform a dinitrogen reduction to ammonia [6]. Ferredoxin dependent enzymes such as cytochrome P450, benzoyl-CoA reductase, and nitrogenase play crucial roles in these metabolic processes [1, 4–8]. In contrast to oxygenic phototrophs and green sulfur bacteria, the photosynthetic reaction center of *R. palustris* cannot reduce Fd directly. Therefore, other enzymatic processes participate in the Fd reduction [6, 9]. In the *R. palustris* CGA009 genome, genes encoding two ferredoxin-NAD(P)$^+$ oxidoreductases ([EC 1.18.1.1], [EC 1.18.1.2], FNR), one putidaredoxin reductase homologue (PdR,[7]), one putative pyruvate-ferredoxin oxidoreductase (RPA1224-1228), and one bifurcation-type Fd reductase (FixABCX, RPA4602-4605, [6]), as well as more than six Fds have been annotated [1, 6, 8]. The roles of the genes and their protein products have been studied using genetic and biochemical approaches. Some Fd genes are located inside the functional gene clusters and their interactions with Fd-dependent enzymes in the same cluster have been investigated, such as nitrogen fixation (fdxB (RPA4612), fdxN (RPA4629), fer1 (RPA4631), [6]), anaerobic aromatic compound degradation (*budB*, RPA0662,[4, 5]), and cytochrome P450 dependent oxygenation (PuxA, RPA1731, [7]). However, the metabolic link of Fds to other putative partner proteins still requires investigation.

FNR is a soluble flavoprotein that catalyzes the redox reaction between Fd and NAD(P)$^+$/H. FNR and its isozymes, putidaredoxin reductase and adrenodoxin reductase, are widely distributed among almost all organisms and can be categorized into several groups based on structure and phylogeny [10–15]. Interestingly, *R. palustris* possesses two FNR genes each of which encodes different types of FNR, designated here as bacterial NADPH-thioredoxin reductase (TrxR)-type FNR (RPA3954, [16]) and plant-type FNR (RPA1578), in addition to one putidaredoxin reductase (PdR) homologue gene (RPA3782). Studies of their protein products have revealed differences in their affinities toward NADH/NADPH and Fds; the homologue of plant-type FNR (RPA1578) from *Rhodobacter capslatus* and TrxR-type FNR (RPA3954) are NADPH specific [16, 17], whereas the PdR homologue (RPA3782) is NADH specific [7]. TrxR-type FNR has low reactivity toward 2Fe-2S type Fd (RPA3956 (PuxB)) [16], whereas the PdR homologue supports CYP199A2 reduction in the presence of 2Fe-2S type Fds (PuxA and PuxB (RPA1872 and RPA3956, respectively)) [7, 18]. A reactivity with 4Fe-4S type Fds from *R. palustris* has not yet been reported. These results suggest that FNRs and PdR homologues play different physiological roles in the bacterium.

In the previous kinetic studies on TrxR-type FNR, pre-steady state reaction analyses of FNRs from heterotroph *Bacillus subtilis* (*Bs*FNR) and photoautotroph *Chlorobaculum tepidum* (*Ct*FNR) with $NADP^+$/NADPH revealed that the two FNRs are distinctive in their redox properties and reversibility in the reaction with $NADP^+$/NADPH; which would correlate with their physiological role, i.e. catalyzing Fd reduction with NAD(P)H or $NAD(P)^+$ reduction with reduced Fd in vivo [19, 20]. Although the crystal structures of these two TrxR-type FNRs have been determined [21, 22], the mechanism regulating the directionality of the reversible reaction has been uncertain. Among the TrxR-type FNR family, FNRs from alpha proteobacteria, including TrxR-type *Rp*FNR (RPA3954), are also distinctive from *Bs*FNR and *Ct*FNR on the amino acid sequence level. For example, in the C-terminal region that directly interacts with the *re*-face of the isoalloxazine ring moiety of the FAD prosthetic group (Fig. 5), the Tyr residue is predicted to stack on the *re*-face of the isoalloxazine ring portion, whereas His is conserved among those from facultative Firmicutes including *Bs*FNR, and Phe is conserved among those from photoautotrophs green sulfur bacteria including *Ct*FNR. Although our previous work with steady state assays indicated that the substitution of the *re*-face aromatic residue does not result in drastic changes in the reactivity toward $NADP^+$/NADPH [21, 22], pre-steady state studies revealed that the C-terminal residues, other than the aromatic one on the *re*-face, play the role of stabilizing the charge transfer complex during the reaction with $NADP^+$/NADPH [23]. Therefore, from the point of view of structure-function relation, *Rp*FNR are worth investigating and the obtained results would provide information related to its physiological function. In this report, the crystal structure of wild type *Rp*FNR was determined and kinetic analyses of the reactions with $NADP^+$/NADPH were carried out using steady state and pre-steady state approaches with the wild type and mutants on the *re*-face Tyr328 residue.

2. Materials and Methods

2.1 Preparation of WT and mutated *Rp*FNRs

Expression vectors for the mutated RPA3954 gene of *R. palstris* CGA009 (*Rp*FNR) were prepared by the replacement of the codon for Tyr328 with that of His (Y328H), Ser (Y328S), and Phe (Y328F) by QuikChange site directed mutagenesis, utilizing the wild-type (WT) expression vector [16] as the template and the following primer pairs; 5′- GTTGTGTTCCAGTTTACGACCTCGTC -3′ and 5′- GACGAGGTCGTAAACTGGAACACAAC -3′ for Y328F, 5′- GTTGTGTTCCAGCACACGACCTCGTC -3′ and 5′- GACGAGGTCGTGTGCTGGAACACAAC -3′ for Y328H, and 5′- GTTGTGTTCCAGTCTACGACCTCGTC -3′ and 5′- GACGAGGTCGTAGACTGGAACACAAC -3′ for Y328S. The sequence of the open reading frame of the mutated *Rp*FNR gene was verified by DNA-sequencing at the Institute for Genomic Research, Kanazawa University. The plasmids obtained were transformed into *E. coli* Tuner (DE3) pLacI cells (Novagen, Merck-Millipore, Merck KGaA, Germany).

Expression and purification of WT and mutated *Rp*FNRs were performed according to the method for WT *Rp*FNR [16] with the following modifications. The collected *E. coli* Tuner (DE3) pLacI cells were disrupted by sonication in the presence of 1 mM phenylmethylsulfonyl fluoride, 1 mM leupeptin, 1 mM p-aminobenzamizine, and 1 mM n-caproic acid. Following Matrex Red dye affinity gel column chromatography, the FNR-containing fraction was dialyzed against 20 mM tris(hydroxymethyl)aminomethane (Tris)-HCl buffer (pH 8.0) and applied to a Source 30Q anion exchange gel column (18 × 200 mm, GE Healthcare UK Ltd., England) pre-equilibrated with the same buffer. After washing the column with the same buffer, *Rp*FNR was eluted using a gradient of sodium chloride concentrations from 0 to 300 mM in 20 mM Tris-HCl buffer (pH 8.0). After concentrating the FNR-containing fractions by ultrafiltration (YM-10, Merck-Millipore), concentrated FNR solution was applied to a gel permeation chromatography column (Superdex 200 10/300, GE healthcare) using 20 mM Tris-HCl buffer containing 200 mM NaCl as an eluent. Eluted FNR containing fractions were dialyzed against 20 mM 4-(2-hydroxyethyl)-1-piperazineethanesulfonic acid (HEPES)-NaOH buffer (pH 7.0) and stored at −80°C before use.

2.2 Steady-state enzymatic assays

The NADPH diaphorase activity using potassium ferricyanide as the electron acceptor, was measured in 20 mM HEPES-NaOH buffer (pH 7.0) at 25°C under aerobic conditions in the presence of; 5 mM glucose-6-phosphate (G6P; Oriental Yeast Co., Ltd., Tokyo, Japan), 5 U/mL glucose-6-phosphate dehydrogenase (G6PDH, *Leuconostoc mesenteroides*; Biozyme Laboratories, Blaenavon, UK), 8.8–10.2 nM *Rp*FNR, and 1 mM potassium ferricyanide, together with 0–1 mM $NADP^+$ (Oriental Yeast Co., Ltd.). After 1 min incubation except *Rp*FNR in the reagent, reaction was initiated by the addition of *Rp*FNR and monitored by the decrease in absorbance at 420 nm for 1 min using a double beam spectrophotometer (V-560, JASCO Co., Tokyo, Japan). The respective blank assay containing all of the assay reagents except *Rp*FNR was subtracted for turnover rate estimation. Turnover rates are expressed as the number of NADPH molecules consumed by one homodimeric FNR. The Michaelis constant (K_M) and turn over number (k_{cat}) were estimated by nonlinear regression analysis using the Michaelis-Menten equation in Igor Pro software (ver. 6.3, WaveMetrics, Portland, OR, USA). The averages of triplicate measurements were used for the estimation of the Michaelis constant (K_M) and turn over number (k_{cat}) by a nonlinear regression analysis using the Michaelis-Menten equation in Igor Pro software (ver. 6.3, WaveMetrics, Portland, OR, USA). The errors in parameters estimated from fitting are represented as ± standard deviation in Table 1.

2.3 Stopped-flow spectrophotometry

Stopped-flow spectrophotometry was performed using a stopped-flow system with a photodiode array detector (Unisoku Co., Ltd., Osaka, Japan) in a glove box (Unico LTD, Tukuba, Japan) under a

nitrogen atmosphere containing approximately 5% hydrogen. The reaction was initiated by mixing equal volumes of solutions in a single-mixing mode at 10°C in 20 mM HEPES-NaOH buffer (pH 7.0). Transient spectra were recorded every 1 ms. The dead-time of the setup was estimated to be approximately 1 ms [19]. Concentrations of the *Rp*FNR protomers, $NADP^+$, NADPH, and (4*S*-^{2}H)-NADPD are provided as the final concentrations after mixing, unless otherwise noted.

Reduced *Rp*FNR (*Rp*FNR_{red}) was prepared by the addition of sodium dithionite in the presence of methyl viologen followed by an exchange of the solution using a size-exclusion chromatography column (Bio-Gel P4 gel, Bio-Rad Laboratories, CA, USA) as described previously [20]. The concentration of *Rp*FNR_{red} was estimated from the absorbance of the air-reoxidized form.

Data collection and basic arithmetic operations on the transient spectra were performed using Unispec (ver. 2.7, Unisoku Co., Ltd.) and Excel (ver. 16.0, Microsoft Corporation, Redmond, WA, USA) software. The transient absorbances at a single wavelength were fitted to exponential decay functions in Igor Pro software. The values of the absorbance at 460 nm (A_{460}) and 590 nm (A_{590}) in the figures were estimated by subtracting A_{800} to compensate for the signal drift. Global analysis of the transient absorption data was performed with Olis GlobalWorks software (ver. 5.888.179, Olis Inc, USA). The selection of potential kinetic reaction models was made based on the weight values, and the spectral and kinetic eigenvectors of the components were estimated by a singular value decomposition analysis. Model validity was assessed by kinetic and overall standard deviations of the fitting. In both single wavelength and global analyses, the averages of 4 or 5 replicate measurements were utilized for the estimation of kinetic parameters in a nonlinear regression analysis. The errors in kinetic parameters estimated from fitting are indicated as ± standard deviation in Tables 2 and 3.

2.4 Crystallization and structural analysis

The purified WT *Rp*FNR was concentrated to approximately 8.0 mg mL^{-1} with Tris-HCl buffer pH 7.8 containing 200 mM NaCl. The crystallization conditions for *Rp*FNR were screened using the hanging-drop vapor diffusion method at 293 K. Refinement of the crystallization conditions showed that the best crystal was obtained using 25 % PEG 3350, 0.1 M HEPES-NaOH pH 7.0, 0.1 M ammonium iodide, and 5 mM DTT as a precipitant. For data collection under cryogenic conditions, crystals were briefly soaked in a reservoir solution containing 15 % (v/v) glycerol, mounted in a nylon loop, and flash-cooled in a stream of gaseous nitrogen at 100 K. Diffraction data from crystals of WT *Rp*FNR were collected by the oscillation method ($\Delta\varphi = 1.0^o$) using synchrotron radiation at beamline NW-12 of the Photon Factory (Tsukuba, Japan). The data were processed and scaled using the HKL2000 program package [24].

The calculated Matthews coefficient (V_M= 2.37 $Å^3$/Da, solvent content 48.2%) indicates that the crystal consists of two molecules per asymmetric unit. For phasing, we carried out a molecular replacement method with the program Molrep in the CCP4 program suite [25]. In initial calculations

using the whole structure of *Ct*FNR chain A or B as a search model, no comprehensive result was obtained. We assumed to be due to the difference in the domain orientation between *Ct*FNR and *Rp*FNR. The phase determination was succeeded using the structure of the FAD-domains of the *Ct*FNR dimer (PDB ID: 3AB1). Model building and refinement were performed using the program Coot and Refmac5 in the CCP4 suite [26, 27]. Finally, TLS refinements were carried out using Refmac5 after adding solvent molecules. In the final electron density map, 51 water molecules were assigned in the asymmetric unit. The *R*-factor of the final model is 0.218 (R_{free} = 0.260). The data collection and refinement statistics are summarized in Table 4. The atomic coordinates and structure factors have been deposited in the Protein Data Bank under the accession code 5YGQ. All figures were generated using PyMOL [28].

2.5 Miscellaneous methods

UV-visible absorption spectra were measured with a double beam spectrophotometer (V-560, JASCO) at 25°C. $NADP^+$ titration was performed in 20 mM HEPES-NaOH buffer (pH 7.0) at 25°C. The difference spectra were obtained by subtracting the control spectrum recorded prior to the addition of $NADP^+$ from the experimentally obtained spectra after correcting for volume changes. Dissociation constant (K_d) values were calculated according to a previous report [29].

SDS-PAGE analysis was performed on a 12% acrylamide gel visualized with Coomassie Brilliant Blue R-250 (AE-1340 EzStain AQUA, ATTO CORP., Japan). The molecular weight marker (Precision Plus Protein Standard) was purchased from Bio-Rad Laboratories.

The molecular masses of the native forms of the enzymes were deduced by gel-permeation chromatography on a Superdex-200 10/300 column (GE Healthcare UK Ltd.) at a flow rate of 0.25 mL min^{-1} using 20 mM Tris-HCl buffer (pH 8.0) containing 200 mM NaCl as the eluent and molecular mass standards purchased from Sigma-Aldrich (Kit for Molecular Weights 12,000–200,000, MWGF200; St Louis, MO, USA).

Absorption coefficients for mutated *Rp*FNRs were determined using the method described in a previous report [30]. An extinction coefficient of 11.3 mM^{-1} cm^{-1} at 450 nm was used for estimation of the FAD concentration.

(4*S*-^{2}H)-NADPD (the deuterated form of NADPH, referred to hereafter as *S*-NADPD) was prepared according to the method described in a previous report [19].

Protein and substrate concentrations were determined using the following extinction coefficients: WT *Rp*FNR (ε_{466} = 10.8 mM^{-1} cm^{-1}, [16]), Y328F *Rp*FNR (ε_{461} = 11.7 mM^{-1} cm^{-1}), Y328H *Rp*FNR (ε_{460} = 11.9 mM^{-1} cm^{-1}), Y328S *Rp*FNR (ε_{459} = 12.8 mM^{-1} cm^{-1}), potassium ferricyanide (ε_{420} = 1.02 mM^{-1} cm^{-1}), and NADPH (ε_{340} = 6.2 mM^{-1} cm^{-1}). $NADP^+$ concentration was determined from the reduced form in the presence of excess G6P and G6PDH.

3. Results

3.1 Molecular mass and spectroscopic properties

Y328F, Y328H, and Y328S *Rp*FNR mutants were purified to homogeneity as judged by sodium dodecyl sulfate poly acrylamide gel electrophoresis (SDS-PAGE) analysis (Fig. S1). Estimation of the apparent molecular masses of mutated *Rp*FNRs provided mass values of 38 kDa on SDS-PAGE, and 67 or 69 kDa on gel-permeation chromatography (Table 1).

The UV-visible absorption spectra of Y328F, Y328H, and Y328S *Rp*FNRs exhibited FAD transition bands I and II in the visible to near-UV region with absorption maxima at 456–461 nm and 378–381 nm, respectively (Fig. 1A). The wavelengths of the absorption maxima of flavin transition band I for the Y328 mutants shifted toward shorter wavelengths compared with that of the WT (Fig. 1A). The absorption coefficients of mutated *Rp*FNRs at the λ_{max} of the flavin transition band I (456–461 nm) exhibited a significant increase compared with that of WT *Rp*FNR (Fig. 1A, Table 1).

3.2 Steady-state assays with $NADP^+$/NADPH

Addition of $NADP^+$ to the WT *Rp*FNR solution induced red-shifts and a decrease in the intensity of the flavin absorption bands, which produced peaks with maxima at 510 and 472 nm, and troughs with minima at 482 and 455 nm on the difference spectrum (Fig. 1B). The addition of $NADP^+$ to mutated *Rp*FNR solution also induced red-shifts and a decrease of the absorption band intensity, resulting in peaks with maxima at 508–510 nm and 472–474 nm, and troughs with minima at 482–484 and 453–454 nm (Fig. 1B). As the addition of $NADP^+$ provided similar spectra for all of the *Rp*FNRs (not shown), the extent of the blue-shift of the absorption band before addition (Fig. 1A) related positively to the absorption intensity of the difference spectra (Fig. 1B, C). The magnitude of the absorbance changes on the difference spectra, $\Delta A_{508\text{-}510}$ *minus* $\Delta A_{483\text{-}484}$ for WT and mutated *Rp*FNRs saturated with increasing $NADP^+$ concentration (Fig. 1C). The estimated K_d values for $NADP^+$ of Y328F and Y328S *Rp*FNRs were significantly smaller than that of WT *Rp*FNR (Table 1).

The reactivity of the WT and mutated *Rp*FNRs with NADPH was evaluated by diaphorase activity using ferricyanide as the electron acceptor (Table 1). Y328H *Rp*FNR provided a similar k_{cat} value but the K_M value for NADPH was slightly smaller than that of the WT. Both the K_M and k_{cat} values of Y328F and Y328S *Rp*FNRs exhibited a substantial decrease compared with those of WT *Rp*FNR (Table 1). The resulting k_{cat}/K_M values of the mutated *Rp*FNRs increased compared with that of WT *Rp*FNR (Table 1).

3.3 Pre-steady state reaction of WT RpFNR

3.3.1 Pre-steady state reaction of oxidized WT RpFNR with NADPH/S-NADPD

The reaction of 9.4 μM WT *Rp*FNR_{ox} with 100–500 μM NADPH or 100 μM *S*-NADPD was measured by stopped-flow spectrophotometry (Fig. 2A, B). Mixing *Rp*FNR_{ox} with 100 μM NADPH

resulted in a slight drop in the absorbance of flavin absorption band I within the dead-time of the instruments (spectrum at 0 ms in Fig. 2A) followed by a gradual decrease with time (Fig. 2A). In the charge transfer (CT) absorption band region [19, 20, 31–33], the absorption band centered at around 590 nm appeared in the first spectrum after mixing (Fig. 2A). The absorbance of this band had a maximum intensity at 3 ms, which decreased with time (Fig. 2A, S2a). At 200 ms, the absorbance of both band regions settled (Fig. 2A, B, S2a). The remaining oxidized *Rp*FNR at 200 ms was estimated to be 31% (Fig. 2A).

Upon mixing with 100 μM *S*-NADPD in place of NADPH, the absorbance of flavin absorption band I also exhibited a drop in the initial spectrum after mixing and the following absorption change continued for a longer period (trace e in Fig. 2B, S2b). The absorbance in the CT band region also showed a rapid increase within the dead time, reaching a maximum intensity at around 5 ms, then decreased with time (Fig. S2a).

Global analysis of the time-resolved absorption spectra implied that the reaction with NADPH was approximated by a two-step sequential reaction model (A→B→C [fast/slow]) (inset of Fig. 2A). Single wavelength analysis at 460 nm also supported the approximation with the same model (red lines in Fig. 2B). The two analyses resulted in similar rate constants (Table 2). In this manuscript, kinetic components are designated as phase I (A→B) and phase II (B→C) in order of rate from fastest to slowest.

The observed rate constant of phase I (k_I) nears the upper limit of the detection of the instruments (400–500 s^{-1}, Table 2). Its values were in the same range as the NADPH concentrations used (100–500 μM). *Δ*absorbance of phase I (ΔA_I) was almost independent of NADPH concentration (Table 2).

The observed rate constant of phase II (k_{II}) decreased from 106 to 77 s^{-1} with increasing NADPH concentration (Table 2). The amplitude of phase II (ΔA_{II}) increased with increasing NADPH concentration (Table 2).

Mixing with *S*-NADPD instead of NADPH decelerated the absorption change (trace e in Fig. 2B). In the single wavelength analysis at 460 nm, fitting with a one-step reaction model (Fig. 2B, Table 2) gave a similar deviation value to that with a two-step sequential reaction model. When a two-step sequential reaction model was applied, the resulting rate constant of phase I (52 ± 1.5 s^{-1}) was close to that of phase II (18 ± 4 s^{-1}). Global analysis of the transient spectra in the 0 to 200 ms time period provided the best approximation with a two-step sequential reaction model because a rapid increase in the CT band region occurred within several ms of mixing (Table 2, Fig. S2b).

3.3.2 Pre-steady-state reaction of WT RpFNR$_{red}$ with NADP$^+$

In the 20 mM HEPES-NaOH buffer at 10°C, reduced WT *Rp*FNR exhibited an absorption band with a peak centered at around 440 nm (bold line in Fig. 2C). After mixing 11.9 μM WT *Rp*FNR$_{red}$ with 100 μM $NADP^+$, the flavin absorption band I and CT band appeared within the dead time

(spectrum at 0 ms in Fig. 2C). The absorbance of flavin absorption band I increased continually with time, whereas that of the CT band reached a maximum at around 7 ms then decreased gradually with time (Fig. 2C, D, Fig. S2c). Within 2000 ms of mixing, the absorbance of both band regions became almost constant (Fig. 2C, D, Fig. S2c). The amount of oxidized *Rp*FNR at 2000 ms was estimated to be approximately 57% (Fig. 2C).

Global analysis of the time-resolved absorption spectra implied that the mixing reaction with $NADP^+$ could be approximated by a two-step sequential reaction model (A→B→C [fast/slow], Fig. 2C inset). Single wavelength analysis at 460 nm supported this approximation (Fig. 2D, Table 3). With increasing $NADP^+$ concentration, ΔA_I and k_I at 100–500 μM $NADP^+$ were almost unchanged, whereas k_{II} and ΔA_{II} decreased and increased, respectively (Table 3).

3.4 Pre-steady state reaction of Tyr328 mutants

3.4.1 Pre-steady-state reactions of oxidized Tyr328 mutants with NADPH/S-NADPD

The reaction of 8.9–9.7 μM mutated *Rp*$FNRs_{ox}$ with 100 μM NADPH resulted in a rapid drop of the absorbance of flavin absorption band I within the dead time (Fig. 3A–F). *Δ*absorbance of the drop for Y328F and Y328S *Rp*FNRs was significantly larger than that for WT *Rp*FNR (Fig. 3A, E). The subsequent gradual decrease of the band became stable within 200 ms. At 200 ms after mixing with 100 μM NADPH, the amounts of remaining Y328F, Y328H, and Y328S *Rp*$FNRs_{ox}$ were comparable with the amount of remaining WT (37%, 28%, and 32%, respectively, vs. 31% (WT), Fig. 3A, C, E).

The transition of A_{460} was approximated by a two-step sequential reaction model (red lines in Fig. 3B, D, F). Global analysis also provided a best approximation with the same model (insets in Fig. 3A, C, E) giving similar rate constant values (Table 2). For all of the mutants, ΔA_I was hardly affected by the NADPH concentration used (100–500 μM). For k_I it should be noted that the lower A_{460} in 100 μM NADPH than in 100 μM *S*-NADPD at 0 ms for Y328S mutant (Fig. 3F), indicated that the reaction was too rapid to monitor the whole absorption change completely, leading to errors for the estimation of k_I.

The k_{II} and ΔA_{II} of Tyr328 mutants exhibited an NADPH concentration dependent decrease and increase, respectively (Table 2). The k_{II} values for Y328F and Y328S *Rp*FNRs were substantially lower than those for WT and Y328H *Rp*FNRs (Table 2).

Mixing with *S*-NADPD lowered the k_I values as observed in the measurement of WT *Rp*FNR (Fig. 3B, D, F). In the case of Y328H *Rp*FNR there was a rapid increasing phase in the CT band region, resulting in the detection of a rapid phase in the global analysis as was observed for WT *Rp*FNR (Fig. 3C, Table 2), whereas a comparable phase was almost undetectable for Y328F and Y328S mutants (Fig. 3A, E, Table 2).

3.4.2 Pre-steady-state reactions of reduced Tyr328 mutants with $NADP^+$

In the reduced form Y328H *Rp*FNR exhibited an absorption band with a maximum at ~440 nm (Fig. 4C), while the wavelength of the absorption maxima of Y328F and Y328S *Rp*FNRs$_{red}$ shifted toward shorter wavelengths (420 and 410 nm, respectively) (Fig. 4A, E).

Mixing mutated *Rp*FNRs$_{red}$ (8.7–11 μM) with 100 μM $NADP^+$ resulted in an appearance of both flavin absorption band I and a CT band within the dead time (Fig. 4A, C, E). A broad absorption band beyond 700 nm was observed in the absorption spectra of Y328F and Y328S *Rp*FNRs at 0 ms (Fig. 4A, E). In contrast, the absorbance over 700 nm was not as intense in the transient spectra of WT *Rp*FNR (Fig. 2C). At 2000 ms, the absorbance change of Y328H *Rp*FNR settled, whereas the absorption change of Y328F and Y328S *Rp*FNRs continued. The amount of oxidized *Rp*FNR at 2000 ms was estimated to be 56% for Y328F *Rp*FNR, 48% for Y328H *Rp*FNR, and 51% for Y328S *Rp*FNR at 100 μM $NADP^+$ (Fig. 4A, C, E).

A_{460} of all mutated *Rp*FNRs in the 0–2000 ms period could be approximated by a two-step sequential reaction model (red lines in Fig. 4B, D, F). The global analysis also confirmed this approximation (inset of Fig. 4A, C, E, Table 3). For all mutants k_I was near the limit of detection, as was also found for WT *Rp*FNR. The k_{II} value for Y328H was larger than those of the other mutants, but smaller than that of WT *Rp*FNR, at the same $NADP^+$ concentrations (Table 3).

3.5 Crystal structure of WT RpFNR

Two *Rp*FNR molecules in the asymmetric unit formed a homodimer (Table 4, Fig. 5B). Each protomer was composed of two typical dinucleotide-binding Rossman fold domains; the one for the FAD-binding consisted of the two discontinuous amino acid residues from 2 to 122 and from 255 to 342, and the other for the $NADP^+$/NADPH-binding consisted of the residues from 127 to 250 (Fig 5A and B). Superposition of each domain of the protomers yielded rmsd values of 0.070 Å for the FAD-binding domain (168 Cα atoms) and 0.185 Å for the NADPH-binding domain (92 Cα atoms). Superposition of the FAD-binding domains of the protomers revealed the difference in the relative position of the $NADP^+$/NADPH-binding domain to the FAD-binding domain between protomers. The NADPH-binding domains were able to overlap each other by rotation of approximately 16.5° around the hinge region comprising the two β-strands, β9 and β16 (Fig. 5A, C). *Rp*FNR has amino acid sequence and structural homology with *Bs*FNR (PDB ID: 3lzw) and *Ct*FNR (PDB ID: 3ab1) (Fig. 5A). The rmsd values of the FAD-binding domain of *Rp*FNR against those of *Bs*FNR and *Ct*FNR were 0.812 Å and 0.817 Å, respectively. The rmsd values of the NADPH-binding domain of *Rp*FNR against those of *Bs*FNR and *Ct*FNR were 0.707 Å and 0.873 Å, respectively.

As described in our previous paper on *Ct*FNR [22], altering the orientation of the NAD(P)H-binding domain toward the FAD-binding domain induced the distortion of the trajectory of the residues in the $NAD(P)^+$/H-binding domain. In *Rp*FNR, flexibility between the two domains resulted in a clear difference in the torsion angles in the hinge region (Arg128-Lys148). The relative orientation of the

two domains in *Rp*FNR also differed from those in *Bs*FNR and *Ct*FNR (Fig. 5C). Upon superposition of the FAD-binding domains of these TrxR-type FNRs and *Ec*TrxR, $NADP^+$/H-binding domains of two protomers of the *Rp*FNR dimer rotated in opposite direction of the Flavin-reducing (FR) form in the *Ec*TrxR crystal [34] compared with those of *Bs*FNR and *Ct*FNR in the crystal (Fig. 5C).

In the FAD-binding domain, one FAD molecule is non-covalently bound in an open conformation (Fig. 5D). The FAD binding site is highly conserved among the three TrxR-type FNRs (Fig. 5A, D). The O2 and N3 atoms of the isoalloxazine ring form hydrogen bonds with the amide nitrogen of Ile300 and the carboxy oxygen of Asp56, respectively. The ribitol moiety was located within hydrogen-bonding distance to the hydroxyl oxygen of Tyr49, which formed a π-π interaction with the isoalloxazine ring, and to the carboxyl oxygen of Asp289. The pyrophosphate moiety was positioned close to the N-terminus of helix α1 and was stabilized by the dipole of the helix [35]. The pyrophosphate oxygen atoms formed hydrogen bonds with the amide nitrogens of Cys17, Asn44, and Gly121, and Nε of Asn44. The 2'-phosphate of the ribose moiety formed hydrogen bonds with the carboxy oxygen of Phe124. The adenine ring of the ADP moiety formed hydrogen bonds with the carbonyl oxygen and amide nitrogen of Val89. In addition to these interactions, the C-terminal extension region was also involved in the recognition of FAD.

The C-terminal extension region (Tyr317-Asn342) involving helix α7 showed a unique construction that was not observed in TrxRs but was conserved in TrxR-type FNRs (Fig. 5A, B, D, E). Crystal structure analysis and amino acid sequence alignment revealed that this region extended beyond helix α6 in the dimer interface of the FAD-binding domain and covered the *re*-face of the isoalloxazine ring portion of FAD bound to the other subunit (Fig. 5B, D, E). The phenyl group of Tyr328 located at the N-terminal of helix α7 stacked nearly parallel to the *re*-face of the isoalloxazine ring with a distance of 3.5 Å between the centroid of both rings. In contrast to the other TrxR-type FNRs, the hydroxyl oxygen of Tyr328 formed a hydrogen bond with the main chain carbonyl oxygen of Lys298. In addition, the hydroxyl oxygen atoms of Thr329 and Thr340, and amide nitrogen of Thr340 were located within hydrogen-bonding distance of the O4 atom of the isoalloxazine ring portion. These hydrogen bonds contribute to maintaining the position of the C-terminal extension region on the FAD-binding domain.

Although we could not determine the structure of *Rp*FNR in a substrate bound form, the $NADP^+$ bound form has been reported in *Bs*FNR [21]. Superposition of the $NADP^+$/NADPH-binding domains of *Rp*FNR and *Bs*FNR indicated that the C-alpha atoms in helix α4 (from Gly163 to Trp169) and loops (from His184 to Arg190 and from Phe248 to Gly250) constituting the $NADP^+$/NADPH binding site in *Rp*FNR, are lying on positions corresponding to those of *Bs*FNR, with the exception of the residues around Arg190, which interact with the 2'-adenosyl phosphate of $NADP^+$ (Fig. 5F). In *Bs*FNR, the side chain of Tyr246 is stacked on the adenylate ring portion of $NADP^+$ [21]. In *Rp*FNR, although the $NADP^+$/NADPH-binding site is vacant, Phe249 is located at the corresponding position (Fig. 5F).

4. Discussion

4.1 Spectroscopic properties

The three purified Tyr328 variants of *Rp*FNR had an apparent molecular mass corresponding to a homodimeric form similar to WT *Rp*FNR (Table 1) [16]. In the UV-vis spectra, substitution for Tyr328 induced a blue-shift of the flavin absorption bands (Fig. 1A). The substitution for the corresponding *re*-face aromatic residues in *Bs*FNR (His324) and *Ct*FNR (Phe337) also resulted in shifts of the flavin absorption bands I and II [21, 22]. In these three TrxR-type FNRs, substitution with the nonaromatic Ser residue resulted in an intense blue-shift [21, 22]. In contrast, the extent of the shift caused by the substitution of the aromatic residues varied for each FNR; the substitution of His and Phe for Tyr328 in *Rp*FNR, and His and Tyr for Phe337 in *Ct*FNR provided a blue shift of flavin absorption band I (Fig.2B, [22]). Flavin absorption band II was centered at around 380 nm and exhibited a substantial blue shift as a result of the substitution for Phe337 in *Ct*FNR (~10 nm, [22]), whereas the shift resulting from the substitution was small in *Rp*FNR (<1 nm, Fig. 1B). In the reduced form, WT and mutated *Rp*FNRs exhibited an intense absorption band with absorption maxima at 410–440 nm, which could be assigned to the $S_0 \rightarrow S_1$ transition [36, 37]. Y328H *Rp*FNR provided a similar peak wavelength to WT whereas those of Y328F and Y328S *Rp*FNRs were blue-shifted (Fig. 2C, 4A, C, E). In the crystal structure of these three FNRs, the trajectory of the peptide backbone of the C-terminal extension; the position and orientation of the *re*-face aromatic residue onto the center piperazine ring of the isoalloxazine ring system; and the hydrogen bonding between the isoalloxazine ring portion and the hydroxyl groups of the Ser/Thr residues in the C-terminal extension, exhibit variations (Fig. 5D, E). This is in contrast to the conservation of the configuration of the residues on the *si*-face side where the Tyr residue (Tyr49 in *Rp*FNR) stacked on the electron dense xylene ring of the isoalloxazine ring system and the Asp residue (Asp56 in *Rp*FNR) hydrogen-bonded with the N3 atom among the three TrxR-type FNRs (Fig. 5D, E). The C-terminal extension in the stacked conformation may participate in the formation of a transient electron transfer complex and/or an efficient electron transfer reaction with a protein substrate [38]. However, the details are uncertain and require further investigation. For plant-type FNR, substitution for C-terminus Tyr resulted in nonfatal but substantial changes in the electron transfer reaction with Fd [39].

4.2 Steady state assay

In the steady-state assays with $NADP^+$ and NADPH, the K_d and K_M values of the mutated *Rp*FNRs decreased significantly compared with those of WT *Rp*FNR (Table 1). In this work, however, the residue located at the NADPH binding site in the $NADP^+$/NADPH-binding domain was not mutated. The decrease in the K_M and K_d values could be due to the changes in the accessibility of the nicotinamide ring portion of $NADP^+$/NADPH to the *re*-face of the isoalloxazine ring portion because

the utilized steady state assays monitor the perturbation of the FAD absorption bands (Fig. 1B), and the redox reaction involving H^- transfer between NADPH and FAD, which requires stacking of the nicotine amide ring portion onto the isoalloxazine ring portion (Table 1) [40, 41]. In the case of plant-type FNRs from Anabaena and pea, the interaction between the C-terminus Tyr residue and the isoalloxazine ring portion destabilizes the stacking of the nicotinamide ring portion of $NADP^+$/NADPH onto the isoalloxazine ring, increasing the observed K_d and K_M values, thereby enhancing the release of $NADP^+$/NADPH, leading to an increase in the turnover rate [42-47]. TrxR-type FNRs conserve the folding with two nucleotide binding domains where FAD and $NAD(P)^+$/H bind to each distinct domain (Fig. 5). Therefore, the productive stacking of the nicotine amide ring portion of $NAD(P)^+$/H onto the isoalloxazine ring portion of FAD requires a large domain motion to promote a hydride transfer as proposed for *Ec*TrxR and TrxR-type FNRs [21–23, 40, 41] (Fig. 5C, F). In this process, the *re*-face residues give a subtle modulation in the interaction between nicotinamide and isoalloxazine portions. In *Rp*FNR, Tyr328 reduces the interaction to optimize the catalytic turnover. The substitution for Tyr328 may weaken the interaction and increase the accessibility of the nicotinamide ring portion, resulting in decreases in the observed K_M, k_{cat}, and K_d values, in a similar manner as for plant-type FNRs [42-47]. Pre-steady state reaction analysis of *Rp*FNR with $NADP^+$/NADPH revealed details of the difference in kinetic behavior between WT and mutated *Rp*FNRs, which supports this observation as below.

4.3 Pre-steady state reaction of $RpFNR_{ox}$ with NADPH

Mixing with NADPH provided a CT band within the dead-time, which then exhibited its maximum intensity by 3 ms. The NADPH concentration used did not significantly affect the intensity at 0 ms (Fig. S2, S3). In Scheme 1, the Michaelis complex (MC) indicates the conformation where $NADP^+$/NADPH is bound to the $NADP^+$/NADPH-binding domain; however, its nicotine amide ring portion does not stack onto the isoalloxazine ring portion, resulting in no CT absorption band; while the CT complex (CTC) gives an intense CT absorption band due to the stacking of the nicotine amide ring portion onto the isoalloxazine ring portion, allowing hydride transfer between the rings. Scheme 1 indicates that these results are in accordance with the rapid formation of MC-1 before the formation of CTC-1 as previously discussed (Scheme 1) [19, 32, 33].

$$\underset{}{FNR_{ox} + NADPH} \underset{k_{-1}}{\overset{k_{+1}}{\rightleftarrows}} \underset{\text{MC-1}}{FNR_{ox}\_NADPH} \underset{k_{-2}}{\overset{k_{+2}}{\rightleftarrows}} \underset{\text{CTC-1}}{FNR_{ox}\text{-}NADPH} \underset{k_{-3}}{\overset{k_{+3}}{\rightleftarrows}} \underset{\text{CTC-2}}{FNR_{red}\text{-}NADP^+} \underset{k_{-4}}{\overset{k_{+4}}{\rightleftarrows}} \underset{\text{MC-2}}{FNR_{red}\_NADP^+} \underset{k_{-5}}{\overset{k_{+5}}{\rightleftarrows}} FNR_{red} + NADP^+$$

Scheme 1

When *S*-NADPD was used instead of NADPH, the maximum intensity of A_{590} and the interval giving the maximum for A_{590} after mixing increased for WT *Rp*FNR (Fig. 2A, S2a, b). In the case of Y328F and Y328S *Rp*FNRs, as well as *Bs*FNR and *Ct*FNR, the maximum intensity was almost the same and the interval was less than 1 ms with both NADPH and *S*-NADPD (Fig. S3) [19, 20]. Taking the rapid

formation of MC-1 (Scheme 1) and much larger k_{II} value of WT *Rp*FNR than Tyr328 mutants (Table 2) into account, such a delay suggests that the k_2 value is close to the k_3 value in the case of WT *Rp*FNR, whereas the k_2 value is larger than the k_3 value in Y328F and Y328S *Rp*FNRs.

In all *Rp*FNRs, the k_I and ΔA_I values were almost independent of NADPH concentration (Table 2). Mixing with *S*-NADPD instead of NADPH reduced the k_I value (Fig. 3, 4, Table 2). These results allow the estimation that the k_{obs} for the hydride transfer process ($k_3 + k_{-3}$) corresponds to the k_I value or faster ($k_3 + k_{-3} \geq k_I$) [18, 44] (Table 2). The obtained k_I values of 400–500 s^{-1} are comparable to those of *Bs*FNR and *Ct*FNR (~500 s^{-1} and >500 s^{-1}, respectively) [19, 20].

With increasing NADPH concentration, k_{II} decreased and ΔA_{II} increased (Table 2). This NADPH concentration dependence after formation of MC-1 in the system in Scheme 1 can be attributed to the formation of the FNR_{red}_NADPH complex as previously discussed (Scheme 2) [20, 48, 49]. Global

$$FNR_{ox} + NADP^+ \underset{k_{-6}}{\overset{k_{+6}}{\rightleftharpoons}} FNR_{ox}\_NADP^+$$

Scheme 2

analysis indicated that the transition from component B to component C (inset of Fig. 2A and 3A, C, E) involves a decrease in the absorbance of both flavin band I and the CT bands. Considering that after *Rp*FNR_{ox} reduction by NADPH; (1) the release of $NADP^+$ from MC-2 is much faster than from CTC-2 as represented in Scheme 1, and (2) k_5, k_{-5}, k_6, and k_{-6} did not change significantly as a result of the substitution for Tyr328 because no residue at the $NADP^+$/NADPH-binding site in the $NADP^+$/NADPH-binding domain was mutated (Fig. 5A, F); the decrease in k_{II} values caused by the substitution could be due to the change of k_{-4} and k_4 (Scheme 1). That is, the mutation may decelerate the transition from CTC-2 to MC-2 and/or stabilize the formation of CTC-2 at the reaction between CTC-2 and MC-2, leading to a slower replacement of $NADP^+$ with NADPH. Among the other TrxR-type FNR members, *Bs*FNR provided the rapid decay of both flavin absorption band I and the CT band, resulting in a rapid turnover rate in the diaphorase assay [20]. In *Rp*FNR, as k_I (400–500 s^{-1} (two electron transfer per FAD at 10°C)) is larger than k_{cat} in the diaphorase assay (200–400 s^{-1} (one electron transfer per FAD at 25 °C), Table 1), the replacement of $NADP^+$ with NADPH could be the rate determining step in the assay. However, it should be noted that the conformation for MC-2 in which the C-terminal extension stacked on the *re*-face, may be preferential for an electron transfer to the protein substrate [38]. In addition, it has often been reported that the electron acceptor such as ferricyanide or ferredoxin would affect the affinity to $NADP^+$/NADPH [29, 44, 46, 49, 50]. The effect on the conformation and cooperativity of the acceptor should be evaluated to elucidate the rate-limiting step in the steady state assay.

4.4 Pre-steady state reaction of $RpFNR_{red}$ with $NADP^+$

Mixing *Rp*FNR_{red} with $NADP^+$ provided rapid formation of both CTCs within the dead time (Fig. 2, 4, S2, S4). The absorbance of the CT band region reached a maximum intensity by 5–10 ms

(Fig. 2C, 4A, C, E). During this period the absorbance of flavin absorption band I also increased with a similar time constant (phase I in Table 3). Based on the formation of CTC-1 in Scheme 1, the k_I in $NADP^+$ reduction could be extrapolated by following either or both cases. If the absorption coefficient of the CT band for CTC-2 is substantially smaller than that of CTC-1, k_I mainly responds to the transition from CTC-2 to CTC-1; however, if they are comparable, the transition from MC-2 to CTC-2 is responsible for k_I. Because the absorption coefficients of the CTCs were not determined, it could not be elucidated whether the transition from MC-2 to CTC-2 is comparable to or faster than that from CTC-2 to CTC-1. However, in both cases it could be elucidated that the observed rate for the hydride transfer reaction ($k_3 + k_{-3}$) is comparable to or faster than the k_I value (400–500 s^{-1}, Table 3). The rapid appearance of the CT band followed by the rapid oxidation of *Rp*FNR_{red} (400–500 s^{-1}) is in contrast to the results for WT and mutated *Ct*FNRs where no CT band was observed and the k_{obs} value was low (~5 s^{-1}) [20, 23]. The results are also in contrast to those of *Bs*FNR where the k_{-3} value is low (< 20 s^{-1}), although rapid formation of CTC-2 after mixing would have occurred [19]. It should be noted that the pre-steady state kinetic analyses of $NADP^+$ reduction for these three TrxR-type FNRs indicated that the presence of the intense absorption band for the $S_0 \rightarrow S_1$ transition in FNR_{red} accompanied the rapid appearance of the CT band within the dead time. Although the conformation of the isoalloxazine ring portion affects the spectroscopic properties of reduced flavoenzymes, electrostatic interactions and hydrogen bonding also have an effect [36]. The precise understanding of the relationship of this transition band to the conformation of the isoalloxazine ring portion in the hydroquinone form, and the relationship of the conformation of the isoalloxazine ring to the rapid formation of CTC-2, require further study.

An increase in $NADP^+$ concentration to 100–500 μM resulted in a decrease of the k_{II} value and an increase in the ΔA_{II} value (Table 3), which could be accounted for by the formation of the FNR_{red}_NADPH complex (Scheme 3) [19, 20, 48, 49]. The transition from component B to component

$$FNR_{red} + NADPH \underset{k_{-7}}{\overset{k_{+7}}{\rightleftharpoons}} FNR_{red}\_NADPH$$

Scheme 3

C in the global analysis indicates an increase in oxidized *Rp*FNR species and a decrease in CTCs for all of the tested *Rp*FNRs during this process (inset of Fig. 2C and 4A, C, E). In the Tyr328 mutants, the k_{II} value was smaller than that of the WT (Table 3). With similar assumptions that k_1, k_{-1}, k_7, and k_{-7} were not affected by the mutation, and the release of NADPH from MC-1 after *Rp*FNR_{red} oxidation was much faster than that from CTC-1 described above, the results indicate that the transition from CTC-1 to MC-1 would be slowed by the mutation. This observation coincides well with those in mixing *Rp*$FNRs_{ox}$ with NADPH, where the transition from MC-1 to CTC-1 was enhanced by the substitution (section 4.3).

5. Conclusion

In this study, the crystal structure of wild type *Rp*FNR was determined. The obtained structure revealed the presence of a Tyr328 residue on the *re*-face of the isoalloxazine ring portion of the FAD prosthetic group that the nicotine amide ring portion of $NADP^+$/NADPH approaches during hydride transfer. The substitution of Phe, His, or Ser resulted in a substantial increase in the affinity for $NADP^+$ and NADPH; however, the overall turnover rate in the diaphorase assay decreased. Pre-steady state kinetics of the reactions of *Rp*FNR_{ox} with NADPH and *Rp*FNR_{red} with $NADP^+$, confirmed that release and re-association of $NADP^+$/NADPH after hydride transfer were slowed down by the substitution, whereas the rate for the hydride transfer was not significantly affected by it. These results support the observation that the presence of the Tyr residue destabilizes the CT complex, and in turn enhances the catalytic turnover for the whole reaction with $NADP^+$/NADPH.

Acknowledgment

We thank Prof. Tomoo Shiba in Kyoto Institute of Technology, Japan for stimulating discussion and the staff at beamline NW12, Photon Factory, Japan for their help during data collection. This work was supported by JSPS KAKENHI Grant Number JP17K07304 (to DS). We thank Sarah Dodds, PhD, from Edanz Group (www.edanzediting.com/ac) for editing a draft of this manuscript.

Reference

[1] F.W. Larimer, P. Chain, L. Hauser, J. Lamerdin, S. Malfatti, L. Do, M.L. Land, D.A. Pelletier, J.T. Beatty, A.S. Lang, F.R. Tabita, J.L. Gibson, T.E. Hanson, C. Bobst, J.L. Torres, C. Peres, F.H. Harrison, J. Gibson, C.S. Harwood, Complete genome sequence of the metabolically versatile photosynthetic bacterium *Rhodopseudomonas palustris*, Nat. Biotechnol. 22 (2004) 55-61.

[2] F.E. Rey, Y. Oda, C.S. Harwood, Regulation of uptake hydrogenase and effects of hydrogen utilization on gene expression in *Rhodopseudomonas palustris*, J Bacteriol. 188 (2006) 6143-6152.

[3] C.S. Harwood, J. Gibson, Anaerobic and aerobic metabolism of diverse aromatic compounds by the photosynthetic bacterium *Rhodopseudomonas palustris*, Appl. Environ. Microbiol. 54 (1988) 712-717.

[4] P.G. Egland, D.A. Pelletier, M. Dispensa, J. Gibson, C.S. Harwood, A cluster of bacterial genes for anaerobic benzene ring biodegradation, Proc. Natl. Acad. Sci. U S A. 94 (1997) 6484-6489.

[5] M. Boll, G. Fuchs, Identification and characterization of the natural electron donor ferredoxin and of FAD as a possible prosthetic group of benzoyl-CoA reductase (dearomatizing), a key enzyme of anaerobic aromatic metabolism, Eur. J. Biochem. 251 (1998) 946-954.

[6] K.R. Fixen, N.P. Chowdhury, M. Martinez-Perez, S. Poudel, E.S. Boyd, C.S. Harwood, The path of electron transfer to nitrogenase in a phototrophic alpha-proteobacterium, Environ. Microbiol. 20 (2018) 2500-2508.

[7] F. Xu, S.G. Bell, Y. Peng, E.O.D. Johnson, M. Bartlam, Z. Rao, L.L. Wong, Crystal structure of a ferredoxin reductase for the CYP199A2 system from *Rhodopseudomonas palustris*, Proteins. 77 (2009) 867-880.

[8] S.G. Bell, N. Hoskins, F. Xu, D. Caprotti, Z. Rao, L.L. Wong, Cytochrome P450 enzymes from the metabolically diverse bacterium *Rhodopseudomonas palustris*, Biochem. Biophys. Res. Commun. 342 (2006) 191-196.

[9] T. Yamanaka, M.D. Kamen, An NADP reductase, an NADH-dye reductase and a non-haem iron protein isolated from a facultative photoheterotroph, *Rhodopseudomonas palustris*, Biochim Biophys Acta. 131 (1967) 317-329.

[10] E.A. Ceccarelli, A.K. Arakaki, N. Cortez, N. Carrillo, Functional plasticity and catalytic efficiency in plant and bacterial ferredoxin-NADP(H) reductases. Biochim Biophys Acta 1698 (2004) 155-165.

[11] A. Aliverti, V. Pandini, A. Pennati, M. de Rosa, G. Zanetti, Structural and functional diversity of ferredoxin-$NADP^+$ reductases, Arch. Biochem. Biophys. 474(2008) 283-291.

[12] D. Seo, K. Kamino, K. Inoue, H. Sakurai, Purification and characterization of ferredoxin-$NADP^+$ reductase encoded by *Bacillus subtilis yumC*, Arch. Microbiol. 182 (2004) 80-89.

[13] I. Hanukoglu, Conservation of the Enzyme-Coenzyme Interfaces in FAD and NADP Binding Adrenodoxin Reductase-A Ubiquitous Enzyme, J. Mol. Evol. 85 (2017) 205-218.

[14] M. Medina, C. Gómez-Moreno, Interaction of ferredoxin-$NADP^+$ reductase with its substrates: optimal interaction for efficient electron transfer, Photosyn Res 79 (2004) 113-131.

[15] O. Dym, D. Eisenberg, Sequence-structure analysis of FAD-containing proteins, Protein Sci. 10 (2001) 1712-1728.

[16] D. Seo, S. Okabe, M. Yanase, K. Kataoka, T. Sakurai, Studies of interaction of homo-dimeric ferredoxin-NAD(P)$^+$ oxidoreductases of *Bacillus subtilis* and *Rhodopseudomonas palustris*, that are closely related to thioredoxin reductases in amino acid sequence, with ferredoxins and pyridine nucleotide coenzymes, Biochim Biophys Acta. 1794 (2009) 594-601.

[17] I. Nogués, I. Pérez-Dorado, S. Frago, C. Bittel, S.G. Mayhew, C. Gómez-Moreno, J.A. Hermoso, M. Medina, N. Cortez, N. Carrillo, The ferredoxin-NADP(H) reductase from *Rhodobacter capsulatus*: molecular structure and catalytic mechanism. Biochemistry.44 (2005) 11730–11740.

[18] S.G. Bell, F. Xu, E.O. Johnson, I.M. Forward, M. Bartlam, Z. Rao, L.L. Wong, Protein recognition in ferredoxin-P450 electron transfer in the class I CYP199A2 system from *Rhodopseudomonas palustris*, J. Biol. Inorg. Chem. 15 (2010) 315-328.

[19] D. Seo, T. Soeta, H. Sakurai, P. Sétif, T. Sakurai, Pre-steady-state kinetic studies of redox reactions catalysed by *Bacillus subtilis* ferredoxin-NADP$^+$ oxidoreductase with NADP$^+$/NADPH and ferredoxin, Biochim. Biophys. Acta 1857 (2016) 678-687

[20] D. Seo, M. Kitashima, T. Sakurai, K. Inoue, Kinetics of NADP$^+$/NADPH reduction–oxidation catalyzed by the ferredoxin-NAD(P)$^+$ reductase from the green sulfur bacterium *Chlorobaculum tepidum*, Photosyn. Res. 130 (2016) 479-489.

[21] H. Komori, D. Seo, T. Sakurai, Y. Higuchi, Crystal structure analysis of *Bacillus subtilis* ferredoxin-NADP$^+$ oxidoreductase and the structural basis for its substrate selectivity, Prot. Sci. 19 (2010) 2279-2290.

[22] N. Muraki, D. Seo, T. Shiba, T. Sakurai, G. Kurisu, Asymmetric dimeric structure of ferredoxin-NAD(P)$^+$ oxidoreductase from the green sulfur bacterium *Chlorobaculum tepidum*: implications for binding ferredoxin and NADP$^+$. J. Mol. Biol. 401 (2010) 403-414.

[23] D. Seo, T. Asano, C-terminal residues of ferredoxin-NAD(P)$^+$ reductase from *Chlorobaculum tepidum* are responsible for reaction dynamics in the hydride transfer and redox equilibria with NADP$^+$/NADPH, Photosyn. Res. 136 (2018) 275-290.

[24] Z. Otwinowski, W. Minor, Processing of X-ray diffraction data collected in oscillation mode, Method. Enzymol, 276 (1997) 307–326.

[25] A. Vagin, A. Teplyakov, Molecular replacement with MOLREP, Acta. Crystallogr. D 66 (2010) 22–25.

[26] P. Emsley, B. Lohkamp, W. Scott, K. Cowtan, Features and development of coot, Acta Crystallogr. D 66 (2010) 486–501.

[27] G.N. Murshudov, P. Skubák, A.A. Lebedev, N.S. Pannu, R.A. Steiner, R.A. Nicholls, M.D. Winn, F. Long, A.A. Vagin, REFMAC5 for the refinement of macromolecular crystal structures, Acta Crystallogr. D 67 (2011) 355–367.

[28] L. Schrödinger, The PyMOL Molecular Graphics System, (2015) Version 1.8 Schrödinger, LLC.

[29] C.J. Batie, H. Kamin, Ferredoxin:$NADP^+$ oxidoreductase. Equilibria in binary and ternary complexes with NADP+ and ferredoxin, J. Biol. Chem. 259 (1984) 8832–8839.

[30] K. Ohnishi, Y. Niimura, K. Yokoyama, M. Hidaka, H. Masaki, T. Uchimura, H. Suzuki, T. Uozumi, M. Kozaki, K. Komagata, T. Nishino, Purification and analysis of a flavoprotein functional as NADH oxidase from *Amphibacillus xylanus* overexpressed in *Escherichia coli*, J. Biol. Chem. 269 (1994) 31418-31423.

[31] V. Massey, R.G. Matthews, G.P. Foust, L.G. Howell, C.H. Williams Jr., G. Zanetti, S. Ronchi, A new intermediate in TPNH-linked flavoproteins. In: Sund H (ed) Pyridine Nucleotide-dependent Dehydrogenases. Springer-Verlag, Berlin, (1970) pp 393–411.

[32] B.W. Lennon, C.H. Williams Jr., Reductive half-reaction of thioredoxin reductase from *Escherichia coli*, Biochemistry 36 (1997) 9464-9477.

[33] J. Tejero, J.R. Peregrina, M. Martínez-Júlvez, A. Gutiérrez, C. Gómez-Moreno, N.S. Scrutton, M. Medina, Catalytic mechanism of hydride transfer bet ween $NADP^+$/NADPH and ferredoxin-$NADP^+$ reductase from *Anabaena* PCC 7119, Arch. Biochem. Biophys. 459 (2007) 79-90.

[34] B.W. Lennon, C.H. Williams Jr., M.L. Ludwig, Twists in catalysis: alternating conformations of *Escherichia coli* thioredoxin reductase, Science 289 (2000) 1190–1194.

[35] W.G. Hol, The role of the alpha-helix dipole in protein function and structure, Prog. Biophys. Mol. Biol. 45 (1985) 149-195.

[36] S. Ghisla, V. Massey, J.M. Lhoste, S.G. Mayhew, Fluorescence and optical characteristics of reduced flavines and flavoproteins, Biochemistry 13 (1974) 589–597.

[37] R.F. Pauszek 3rd, G. Kodali, M.S. Siddiqui, R.J. Stanley, Overlapping electronic states with nearly parallel transition dipole moments in reduced anionic flavin can distort photobiological dynamics, J. Am. Chem. Soc. 138 (2016) 14880-14889.

[38] D. Seo, T. Asano, H. Komori, T. Sakurai, Role of the C-terminal extension stacked on the *re*-face of the isoalloxazine ring moiety of the flavin adenine dinuc leotide prosthetic group in ferredoxin-$NADP^+$ oxidoreductase from *Bacillus subtilis*. Plant Physiol Biochem 81 (2014) 143-148.

[39] I. Nogués, J. Tejero, J.K. Hurley, D. Paladini, S. Frago, G. Tollin, S.G. Mayhew, C. Gómez-Moreno, E.A. Ceccarelli, N. Carrillo, M. Medina, Role of the C-terminal tyrosine of ferredoxin-nicotinamide adenine dinucleotide phosphate reductase in the electron transfer processes with its protein partners ferredoxin and flavodoxin, Biochemistry 43 (2004) 6127-6137.

[40] I. Gudim, M. Hammerstad, M. Lofstad, H.P. Hersleth, The characterization of different flavodoxin reductase-flavodoxin (FNR-Fld) interactions reveals an efficient FNR-Fld redox pair and identifies a novel FNR subclass, Biochemistry 57 (2018) 5427-5436.

[41] G. Waksman, T.S. Krishna, C.H. Williams Jr, J. Kuriyan, Crystal structure of *Escherichia coli* thioredoxin reductase refined at 2 Å resolution. Implications for a large conformational change during catalysis, J. Mol. Biol. 236 (1994) 800-816.

[42] L. Piubelli, A. Aliverti, A.K. Arakaki, N. Carrillo, E.A. Ceccarelli, P.A. Karplus, G. Zanetti, Competition between C-terminal tyrosine and nicotinamide modulates pyridine nucleotide affinity and specificity in plant ferredoxin-$NADP^+$ reductase. J. Biol. Chem. 275 (2000) 10472-10476.

[43] J. Tejero, I. Pérez-Dorado, C. Maya, M. Martínez-Júlvez, J. Sanz-Aparicio, C. Gómez-Moreno, J.A. Hermoso, M. Medina, C-terminal tyrosine of ferredoxin-$NADP^+$ reductase in hydride transfer processes with $NAD(P)^+$/H, Biochemistry 44 (2005) 13477-13490.

[44] D.H. Paladini, M.A. Musumeci, N. Carrillo, E.A. Ceccarelli, (2009) Induced fit and equilibrium dynamics for high catalytic efficiency in ferredoxin-NADP(H) reductases, Biochemistry 48 (2009) 5760-5768.

[45] J.R. Peregrina, A. Sánchez-Azqueta, B. Herguedas, M. Martínez-Júlvez, M. Medina, Role of specific residues in coenzyme binding, charge-transfer complex formation, and catalysis in *Anabaena* ferredoxin $NADP^+$-reductase, Biochim. Biophys. Acta 1797 (2010) 1638-1646.

[46] P. Mulo, M. Medina, Interaction and electron transfer between ferredoxin–$NADP^+$ oxidoreductase and its partners: structural, functional, and physiological implications, Photosyn. Res. 134 (2017) 265–280.

[47] M.A. Musumeci, A.K. Arakaki, D.V. Rial, D.L. Catalano-Dupuy, E.A. Ceccarelli, Modulation of the enzymatic efficiency of ferredoxin-NADP(H) reductase by the amino acid volume around the catalytic site, FEBS J. 275 (2008) 1350-1366.

[48] S. Daff, An appraisal of multiple NADPH binding-site models proposed for cytochrome P450 reductase, NO synthase, and related diflavin reductase systems, Biochemistry 43 (2004) 3929-3932.

[49] C.J. Batie, H. Kamin, Association of ferredoxin-$NADP^+$ reductase with NADP(H) specificity and oxidation-reduction properties, J. Biol. Chem. 261 (1986) 11214-11223.

[50] M. Martínez-Júlvez, M. Medina, A. Velázquez-Campoy, Binding thermodynamics of ferredoxin:$NADP^+$ reductase: two different protein substrates and one energetics. Biophys J. (2009) 96 (2009) 4966-4975.

[51] M.A. Larkin, G. Blackshields, N.P. Brown, R. Chenna, P.A. McGettigan, H. McWilliam, F. Valentin, I.M. Wallace, A. Wilm, R. Lopez, J.D. Thompson, T.J. Gibson, D.G. Higgins, Clustal W and Clustal X version 2.0, Bioinformatics 23 (2007) 2947-2948.

[52] P. Gouet, X. Robert, E. Courcelle, ESPript/ENDscript: Extracting and rendering sequence and 3D information from atomic structures of proteins, Nucleic Acids Res. 31 (2003) 3320-3323.

Figure legends

Fig. 1 (A) Near UV-visible absorption spectra in the air-oxidized form and (B) difference spectra induced by the addition of 1 mM $NADP^+$ of wild type (black broken line), Y328F (red continuous line), Y328H (blue continuous line) and Y328S (green continuous line) *Rp*FNRs. The spectrum was measured in 20 mM HEPES-NaOH buffer (pH 7.0) at 25°C. Absorption coefficient of *Rp*FNR was estimated based on the FAD concentration as described in the Materials and methods section. (C)

$NADP^+$ concentration dependency of the absorbance on the difference spectra. The changes of the absorbance of the difference spectra for wild type (black circle): $\Delta\varepsilon_{508}$ - $\Delta\varepsilon_{483}$, Y328F (red square): $\Delta\varepsilon_{510}$ - $\Delta\varepsilon_{483}$, Y328H (blue triangle): $\Delta\varepsilon_{509}$ - $\Delta\varepsilon_{483}$ and Y328S (green diamond): $\Delta\varepsilon_{509}$ - $\Delta\varepsilon_{484}$ *Rp*FNRs were plotted against $NADP^+$ concentration. Curves were obtained using a reversible one-binding site model [29] with the K_d values in Table 1.

Fig. 2. (A) Transient spectra induced by mixing 9.4 μM wild type *Rp*FNR_{ox} with 100 μM NADPH in 20 mM HEPES-NaOH buffer (pH 7.0) at 10°C. The spectra at 0, 10, 100 and 1000 ms are shown as thin continuous lines, and those at 1, 2, 5, 20, 50, 200 and 500 ms as thin dotted lines from the top to the bottom at 450 nm. The spectrum at 5 ms is colored in red. The spectrum of oxidized wild type *Rp*FNR is shown as a thick continuous line. The arrows indicate the directions of the absorbance changes at the respective wavelengths. The dashed parts of the arrows indicate that absorption change occurred within the dead time (~1 ms). The inset shows the spectrum of each kinetic component resulting from global analysis of the transient spectra with a two-step sequential reaction model (A → B → C [fast/slow]). (B) The time course of A_{460} after mixing wild type *Rp*FNR_{ox} with NADPH or *S*-NADPD. The measurement conditions were the same as those in Fig. 2A except the NADPH concentrations of 0 μM (trace a), 100 μM (trace b), 200 μM (trace c) and 500 μM (trace d), or 100 μM *S*-NADPD (trace e). The data are an average of five replicates. The red lines indicate the fitted curves with a two-component exponential function. The residuals are indicated as black lines (NADPH) and a red line (*S*-NADPD) in the lower figure panel. (C) Transient spectra induced by mixing 11.9 μM reduced wild type *Rp*FNR with 100 μM $NADP^+$ in 20 mM HEPES-NaOH buffer (pH 7.0) at 10°C. The spectra at 0, 10, 100 and 1000 ms are shown as thin continuous lines, and those at 1, 2, 5, 20, 50, 200 and 500 ms as thin dotted lines from the bottom to the top at 450 nm. The spectrum of oxidized and reduced wild type *Rp*FNR are shown as a thick dotted and thick continuous lines, respectively. The arrows indicate the directions of the absorbance changes at the respective wavelengths. The inset shows the spectrum of each kinetic component resulting from global analysis of the transient spectra with a two-step sequential reaction model (A → B → C [fast/slow]). (D) The time course of A_{460} after mixing reduced wild type *Rp*FNR with $NADP^+$. The measurement conditions were the same as those in Fig. 2C, except the $NADP^+$ concentrations of 0 μM (trace a), 100 μM (trace b), 200 μM (trace c) and 500 μM (trace d). The data are an average of four to five replicates. The fitted curves with a two-component exponential function are indicated as red lines. The residuals of the fitting are represented in the lower figure panel.

Fig. 3. (A, C, E) Transient spectra induced by mixing oxidized (A) 9.7 μM Y328F, (C) 8.9 μM Y328H and (E) 9.0 μM Y328S *Rp*FNRs with 100 μM NADPH in 20 mM HEPES-NaOH buffer (pH 7.0) at 10°C. The thin continuous lines from the top to the bottom at 450 nm indicated the spectra at 0, 10,

100 and 1000 ms, respectively. The spectra shown by the thin dotted lines from the top to the bottom at 450 nm correspond to those at 1, 2, 5, 20, 50, 200, 500 and 2000 ms, respectively. The arrows indicate the directions of the absorbance changes at the respective wavelengths. The dashed parts of the arrows indicate that change occurred within the dead time (~1 ms). The inset shows the spectrum of each kinetic component resulting from global analysis of the transient spectra with two-step sequential reaction model (A → B → C [fast/slow]). (B, D, F) The time course of A_{460} after mixing oxidized (B) Y328F, (D) Y328H and (F) Y328S *Rp*FNRs with NADPH and *S*-NADPD. The measurement conditions were the same as those in Fig. 3A, C, E, respectively, except the NADPH concentrations of 0 μM (trace a), 100 μM (trace b), 200 μM (trace c) and 500 μM (trace d), or 100 μM *S*-NADPD (trace e). The data are an average of five replicates. The fitted curves with a two-component exponential function are indicated as red lines. The residuals are indicated as black continuous lines in the lower figure panel.

Fig. 4 Transient spectra induced by mixing reduced (A) 9.4 μM Y328F, (C) 11.0 μM Y328H and (E) 8.7 μM Y328S *Rp*FNRs with 100 μM $NADP^+$. The reaction was performed in 20 mM HEPES-NaOH buffer (pH 7.0) at 10°C. The thin continuous lines from the bottom to the top at 450 nm indicated the spectra at 0, 10, 100 and 1000 ms, respectively. The spectra shown by thin dotted lines from the bottom to the top at 450 nm correspond to those at 1, 2, 5, 20, 50, 200, 500 and 2000 ms, respectively. The spectra of oxidized and reduced *Rp*FNRs are shown as a thick broken and thick continuous lines, respectively. The arrows indicate the directions of the absorbance changes at the respective wavelengths. The dashed parts of the arrows indicate that the changes occurred within the dead time (~1 ms). The inset shows the spectra of kinetic components resulting from global analysis of the transient spectra with two-step sequential reaction model (A → B → C [fast/slow]). (B, D, F) The time course of A_{460} after mixing reduced (B) Y328F, (D) Y328H and (F) Y328S *Rp*FNRs with $NADP^+$. The measurement conditions were the same as those in Fig. 4A, C, E, respectively, except that the $NADP^+$ concentrations of 0 μM (trace a), 100 μM (trace b), 200 μM (trace c) or 500 μM (trace d). The data are an average of five replicates. The fitted curves with a two-component exponential function are indicated as red lines. The residuals are indicated as black lines in the lower figure panels.

Fig. 5

(A) The aligned amino acid sequences of *Rp*FNR(RPA3954), *Ct*FNR(CT1512) and *Bs*FNR(yumC). The positions of the corresponding secondary structures observed in the crystal of *Rp*FNR for molecule 1 (PDB ID: 5YGQ) are indicated at the upper lines. The residues stacking on the *si*-face (Tyr49) and *re*-face (Tyr328) of the isoalloxazine ring portion are indicated with red arrow heads at the bottom line. The position of the residues involved in $NADP^+$/NADPH-biding in the crystal

structure of *Bs*FNR are indicated with blue stars at the bottom line. The residues comprising FAD-binding and $NADP^+$/NADPH-binding domains are boxed with red and green lines, respectively. Alignment of the amino acid sequences is performed on ClustalW [51]. The figure was prepared using ESPript 3.0 [52].

(B) Crystal structure of *Rp*FNR. The chains are depicted by different colors. FAD molecules are shown in a stick model.

(C) Comparison of the domain arrangement of *Rp*FNR, *Bs*FNR, *Ct*FNR and *Ec*TrxR. Each gray allow shows the rotation axis from the left-hand panel to the right-hand panel obtained from domain motion analysis. The residues from Asp164 to Asp168 in *Rp*FNR and corresponding residues in others located in the N-terminal region of 4^{th} helices are colored in orange.

(D) Structure comparison of the FAD binding sites in TxrR-type FNRs. *Rp*FNR is shown in blue (chain A) and teal color (chain B). *Bs*FNR is shown in magenta (chain A) and brown (chain B). *Ct*FNR is shown in green (chain B) and light green (chain A).

(E, F) Superimposition of the local structure around the isoalloxazine ring (E) and the $NADP^+$/NADPH-binding sites (F) of *Rp*FNR with *Bs*FNR bound $NADP^+$. The residues, which interact with FAD and $NADP^+$ are shown in a stick model. The number of the corresponding residues of *Bs*FNR are shown in parenthesis.

Table 1

Enzymatic, spectroscopic and molecular mass properties of WT *Rp*FNR and its Tyr328 mutants.

	WT	Y328F	Y328H	Y328S
NADPH diaphorase with ferricyanide[a]				
K_M for NADPH (μM)	59 ± 4	5.7 ± 0.5	21 ± 1.9	3.5 ± 0.3
k_{cat} (s^{-1})	323 ± 6	186 ± 3	368 ± 7	207 ± 3
k_{cat}/K_M ($\times 10^6$ $M^{-1}s^{-1}$)	5.5 ± 0.1	32.6 ± 0.5	17.5 ± 0.3	59 ± 0.9
K_d for $NADP^+$ (μM) [b]	12 ± 1.1	1.94 ± 0.07	5.9 ± 0.4	0.97 ± 0.07
ε ($mM^{-1}cm^{-1}$ per subunit) / at λ max (nm)	10.8[c] / 466[c]	11.7 / 461	11.9 / 460	12.8 / 459
M_r(gel-permeation/ SDS-PAGE)(kDa)	67 / 38	67 / 38	67 / 38	69 / 38

The values with ± one standard deviation are represented.

a: at 1 mM ferricyanide in 20 mM HEPES-NaOH buffer (pH 7.0) at 25°C.

b: obtained with the data in Figure 1C.

c: from [16]

Table 2

Kinetic constants obtained by the pre-steady state analysis of mixing oxidized WT and Y328 mutants with NADPH/*S*-NADPD

[NADPH]		100 μM[a]	200 μM[a]	300 μM	500 μM[a]	100 μM *S*-NADPD[a]
WT	K_I	380 ± 30 (410 ± 11)	470 ± 30 (430 ± 50)	490 ± 40 (420 ± 50)	460 ± 30 (400 ± 30)	44.7 ± 0.2 (407 ±7)
	ΔA_I	0.023 ± 0.001	0.0231 ± 0.0008	0.0201 ± 0.0008	0.0248 ± 0.0007	0.0450 ± 0.00015
	K_{II}	106 ± 3 (115 ± 2)	93 ± 1.9 (92 ± 6)	87 ± 1.6 (82 ± 3)	77 ± 1.1 (78 ± 2)	(43 ± 1.4)
	ΔA_{II}	0.029 ± 0.0016	0.0322 ± 0.0009	0.0337 ± 0.0007	0.0355 ± 0.0006	-
Y328F	K_I	520 ± 20 (560 ± 10)	600 ± 20 (610 ± 70)	730 ± 30 (630 ± 10)	600 ± 20 (510 ± 70)	72 ± 1 (69 ± 3)
	ΔA_{II}	0.0174 ± 0.0004	0.0158 ± 0.0003	0.0154 ± 0.0003	0.0155 ± 0.0003	0.0303 ± 0.0003
	K_{II}	63 ± 1.5 (67 ± 6)	49.5 ± 0.7 (49 ± 1.8)	42.7 ± 0.5 (43 ± 2)	36.9 ± 0.4 (35 ± 1.4)	12 ± 1.3 (12 ± 1.6)
	ΔA_{II}	0.0154 ± 0.0004	0.0182 ± 0.0002	0.0195 ± 0.00017	0.0220 ± 0.00015	0.0056 ± 0.0003
Y328H	K_I	350 ± 30 (610 ± 12)	410 ± 30 (590 ± 70)	500 ± 20 (560 ± 30)	440 ± 19 (530 ± 50)	69 ± 6 (520 ± 20)
	ΔA_I	0.023 ± 0.0015	0.0186 ± 0.0008	0.0178 ± 0.0005	0.01835 ± 0.0005	0.022 ± 4
	K_{II}	89 ± 3 (112 ± 3)	80 ± 1.6 (93 ± 3)	74.9 ± 0.8 (82 ± 3)	66.1 ± 0.7 (79 ± 5)	31 ± 1.9 (42 ± 1.4)
	ΔA_{II}	0.027 ± 0.0015	0.0326 ± 0.0008	0.0343 ± 0.0004	0.0366 ± 0.4	0.026 ± 0.004
Y328S	k_1	400 ± 19 (390 ± 60)	410 ± 16 (370 ± 60)	450 ± 20 (370 ± 30)	420 ± 18 (438 ± 5)	70 ± 1.4 (68 ± 2)
	ΔA_I	0.0183 ± 0.0005	0.0166 ± 0.0003	0.0153 ± 0.0004	0.0153 ± 0.0003	0.0310 ± 0.0006
	K_{II}	58 ± 1.9 (60 ± 5)	41.3 ± 0.8 (39 ± 2)	40.8 ± 0.8 (38 ± 2)	33.1 ± 0.5 (31.7 ± 0.4)	16 ± 1.6 (15 ± 1.2)
	ΔA_{II}	0.0131 ± 0.0005	0.0142 ± 0.0003	0.0164 ± 0.0003	0.0187 ± 0.0002	0.0068 ± 0.0006

Observed rate constant (k) and amplitude (ΔA) of each phase obtained by a fitting with single- or bi-exponential decay function against A_{460} for 0-100 ms (WT with NADPH) or 0-200 ms (the others) time period are represented with ± one standard deviation. The rate constant values in the parentheses are those obtained by a global analysis with a two-step reaction model (A→B→C [fast/slow]).

a: Data in Fig. 2B (WT), and Fig.3B, D, F (Y328F, Y328H and Y328S, respectively) were utilized for the estimation.

Table 3

Kinetic constants obtained by the pre-steady state analysis of mixing reduced WT and Y328 mutants with $NADP^+$

[$NADP^+$]		100 μM[a]	200 μM[a]	300 μM	500 μM[a]
WT	k_I	**451 ± 5 (310 ± 80)**	**464 ± 6 (340 ± 50)**	**546 ± 6 (380 ± 40)**	**587 ± 6 (418 ± 0.8)**
	ΔA_I	**0.0528 ± 0.0005**	**0.0522 ± 0.0006**	**0.0495 ± 0.0005**	**0.0511 ± 0.0005**
	k_{II}	**14.41 ± 0.09 (14 ± 1.8)**	**10.55 ± 0.05 (11.4 ± 0.6)**	**9.47 ± 0.03 (10.0 ± 0.4)**	**6.96 ± 0.011 (6.9 ± 0.4)**
	ΔA_{II}	**0.01404 ± 0.00007**	**0.01833 ± 0.00006**	**0.02176 ± 0.00004**	**0.02597 ± 0.00003**
Y328F	k_I	**596 ± 6 (400 ± 40)**	**593 ± 7 (380 ± 20)**	**526 ± 8 (390 ± 70)**	**526 ± 9 (420 ± 70)**
	ΔA_I	**0.0459 ± 0.0005**	**0.0421 ± 0.0005**	**0.0373 ± 0.0005**	**0.0373 ± 0.0006**
	k_{II}	**3.01 ± 0.05 (2.7 ± 0.4)**	**2.271 ± 0.007 (2.05 ± 0.07)**	**1.935 ± 0.007 (1.71 ± 0.07)**	**1.476 ± 0.006 (1.31 ± 0.05)**
	ΔA_{II}	**0.00900 ± 0.000016**	**0.01141 ± 0.000015**	**0.01258 ± 0.000017**	**0.01392 ± 0.000019**
Y328H	k_I	**525 ± 5 (400 ± 40)**	**565 ± 6 (420 ± 15)**	**517 ± 4 (350 ± 30)**	**536 ± 5 (400 ± 30)**
	ΔA_I	**0.0454 ± 0.0004**	**0.0452 ± 0.0004**	**0.0486 ± 0.0003**	**0.04766 ± 0.0004**
	k_{II}	**9.08 ± 0.03 (8.6 ± 0.5)**	**6.57 ± 0.016 (6.3 ± 0.11)**	**5.201 ± 0.009 (5.4 ± 0.5)**	**4.093 ± 0.006 (4.01 ± 0.07)**
	ΔA_{II}	**0.01237 ± 0.00003**	**0.01578 ± 0.00003**	**0.01789 ± 0.00002**	**0.02059 ± 0.000018**
Y328S	k_I	**596 ± 6 (410 ± 60)**	**547 ± 7 (370 ± 90)**	**587 ± 8 (420 ± 80)**	**598 ± 8 (380 ± 80)**
	ΔA_I	**0.0410 ± 0.0004**	**0.0378 ± 0.0005**	**0.0371 ± 0.0005**	**0.0358 ± 0.0005**
	k_{II}	**2.313 ± 0.008 (2.11 ± 0.16)**	**1.447 ± 0.007 (1.40 ± 0.06)**	**1.205 ± 0.005 (1.30 ± 0.09)**	**1.137 ± 0.004 (1.11 ± 0.07)**
	ΔA_{II}	**0.00827 ± 0.000013**	**0.01014 ± 0.000015**	**0.01118 ± 0.000016**	**0.01307 ± 0.000016**

Observed rate constant (k) and amplitude (ΔA) of each phase obtained by a fitting with bi-exponential decay function against A_{460} for 0-2000 ms time period are represented with ± one standard deviation. The rate constant values in the parentheses are those obtained by a global analysis with a two-step reaction model (A→B→C [fast/slow]).

a: Data in Fig. 2D (WT) and Fig.4B, D, F (Y328F, Y328H and Y328S, respectively) were utilized for the estimation.

Table 4 Crystallographic data and refinement statistics

	WT *Rp*FNR
Data collection	
X-ray Source	PF AR-NW12
Wavelength (Å)	1.0000
Space group	$P2_12_12_1$
Cell dimensions	
a, b, c (Å)	70.9, 81.2, 122.2
Resolution range (Å)	50.00-2.40 (2.49-2.40)[a]
No. total reflections	187,215
No. unique reflections	27,560 (1,898)[a]
Completeness (%)	98.3 (88.1)[a]
$R_{merge}(I)$ (%)[b]	8.1 (39.9)[a]
$I/\delta I$	8.5 (2.3)[a]
Multiplicity	6.9 (5.1)[a]
Refinement	
Resolution	36.41-2.40
R_{work}/R_{free} (%)	21.8/26.3
No. atoms	
Protein	5195
FAD	106
Water	51
B-factors	
Protein	50.17
FAD	31.91
Water	33.38
R.m.s. deviation	
Bond length (Å)	0.019
Bond angles (º)	2.15
Ramachandran plot	
Favored (%)	96.31
Allowed (%)	3.25
Outliers (%)	0.44

a: Highest resolution shell is shown in parentheses.

b: $R_{merge}(I) = \Sigma|I(k) - \langle I \rangle|/\Sigma I(k)$, with I(k) representing the k value of an intensity measurement of a reflection, <I> the mean intensity value of that reflection, and Σ the summation across all measurements.

Figure 1a

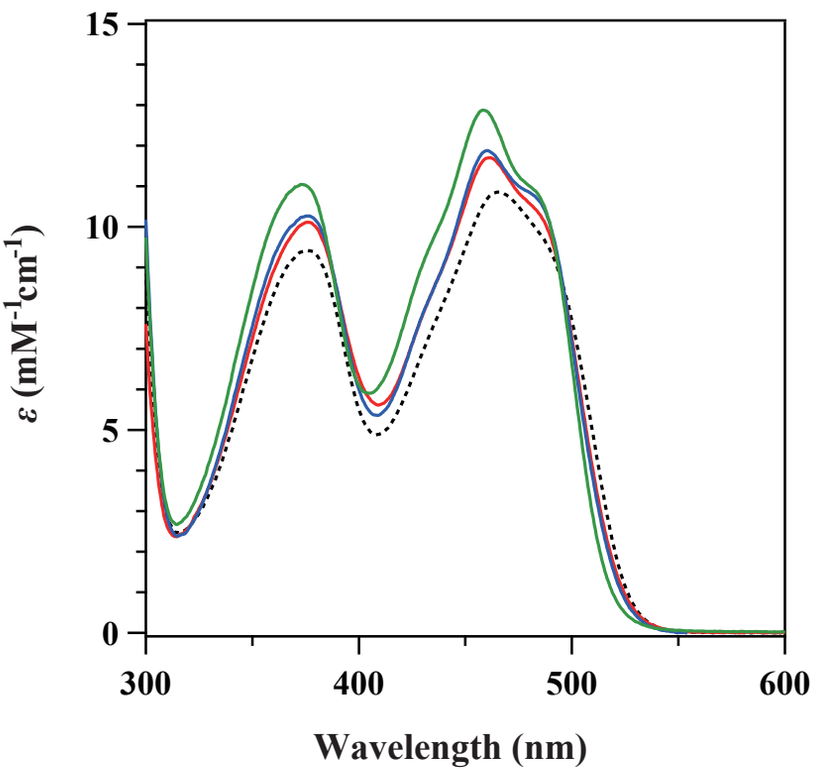

Figure 1b

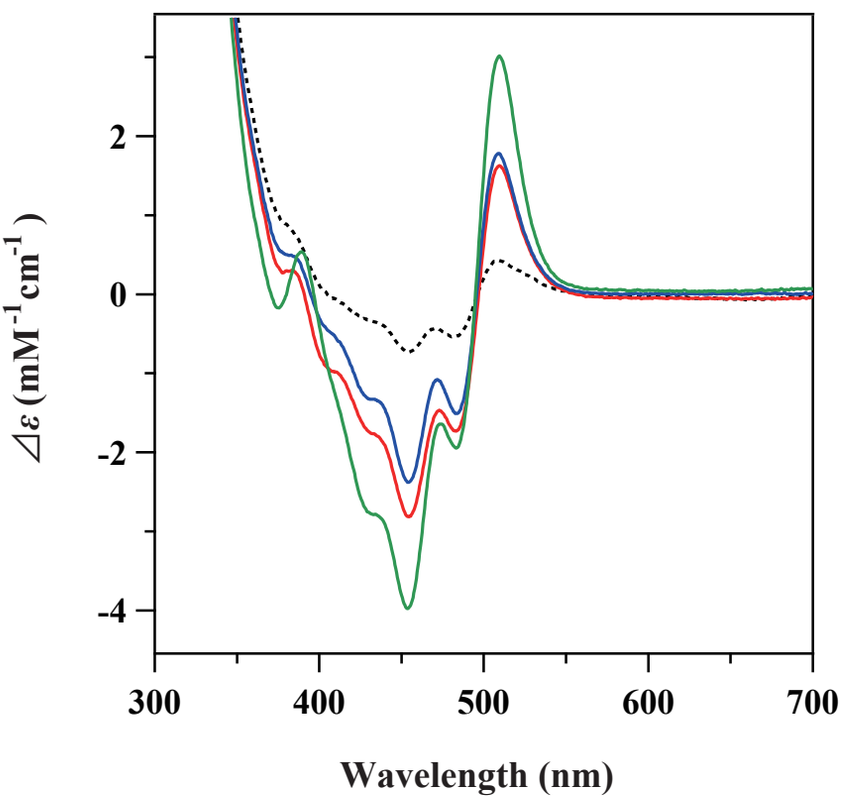

Figure 1c

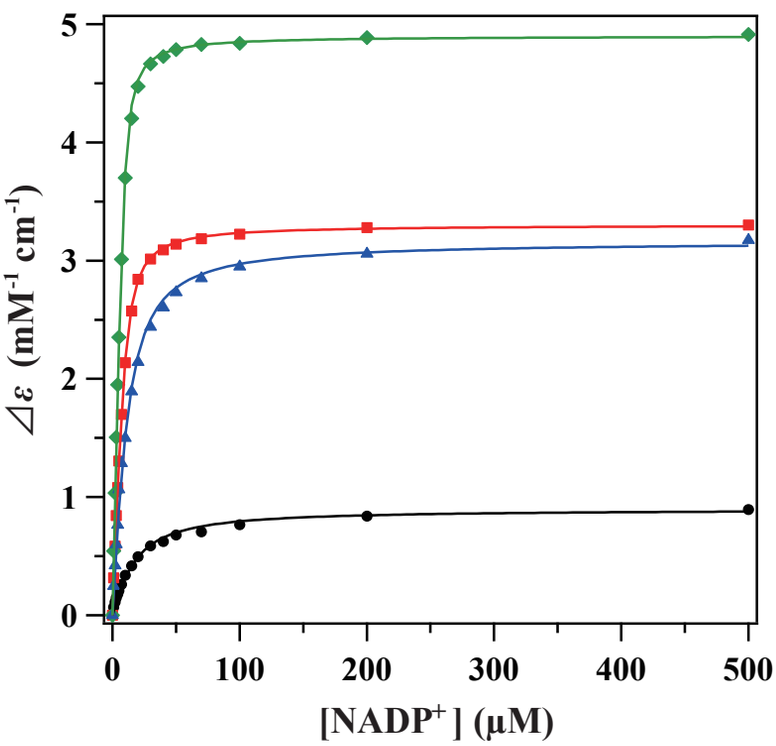

Figure 2A

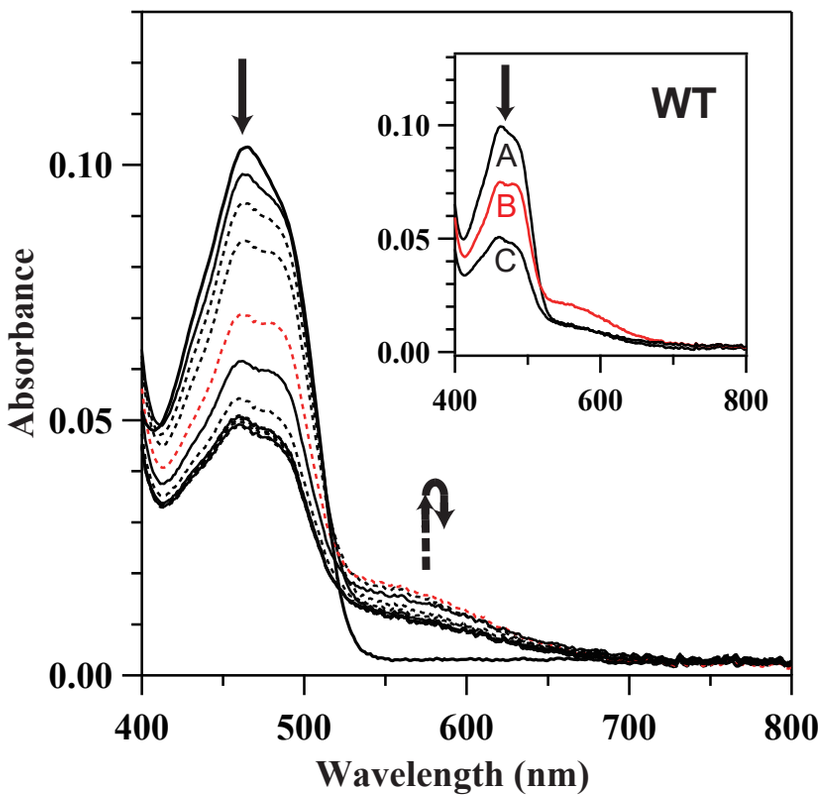
Absorbance
0.10
0.05
0.00
400
500
600
700
800
Wavelength (nm)
WT
A
B
C
0.10
0.05
0.00
400
600
800

Figure 2B

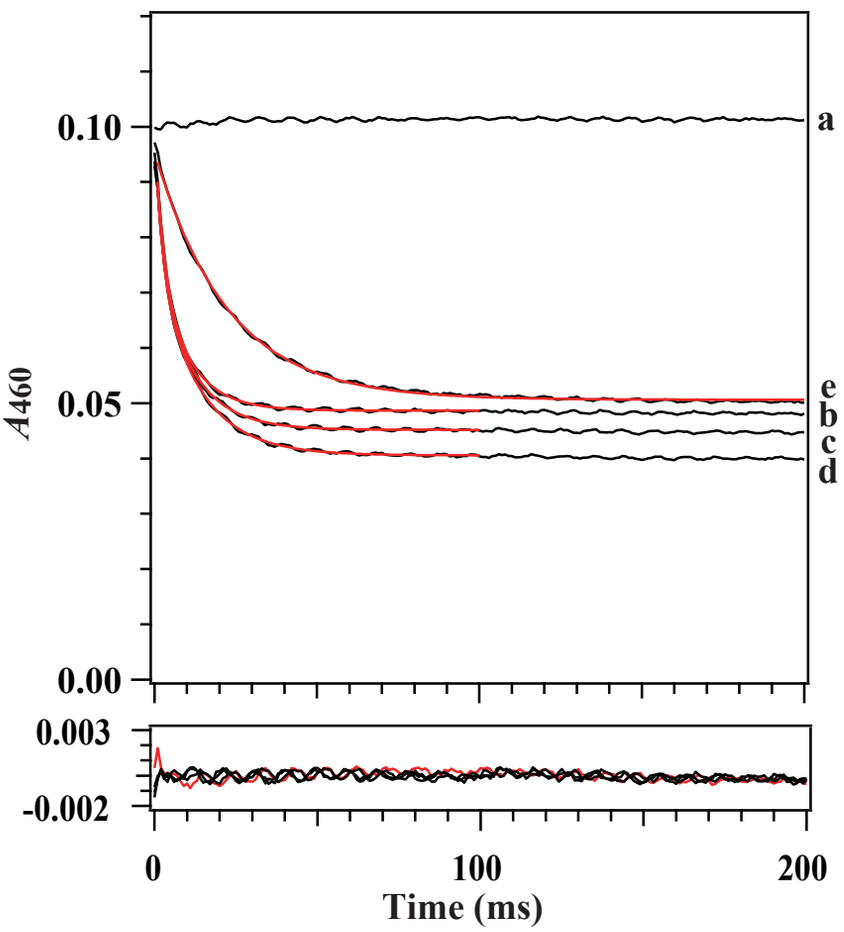

Figure 2c

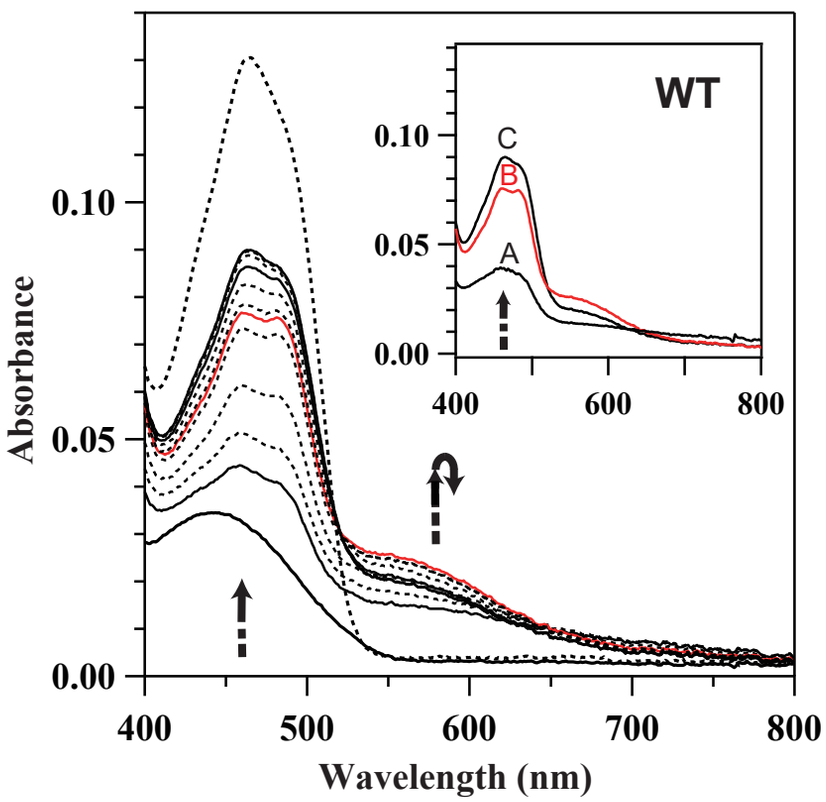
WT
C
B
A
0.10
0.05
0.00
400
600
800
Absorbance
0.10
0.05
0.00
400
500
600
700
800
Wavelength (nm)

Figure 2D

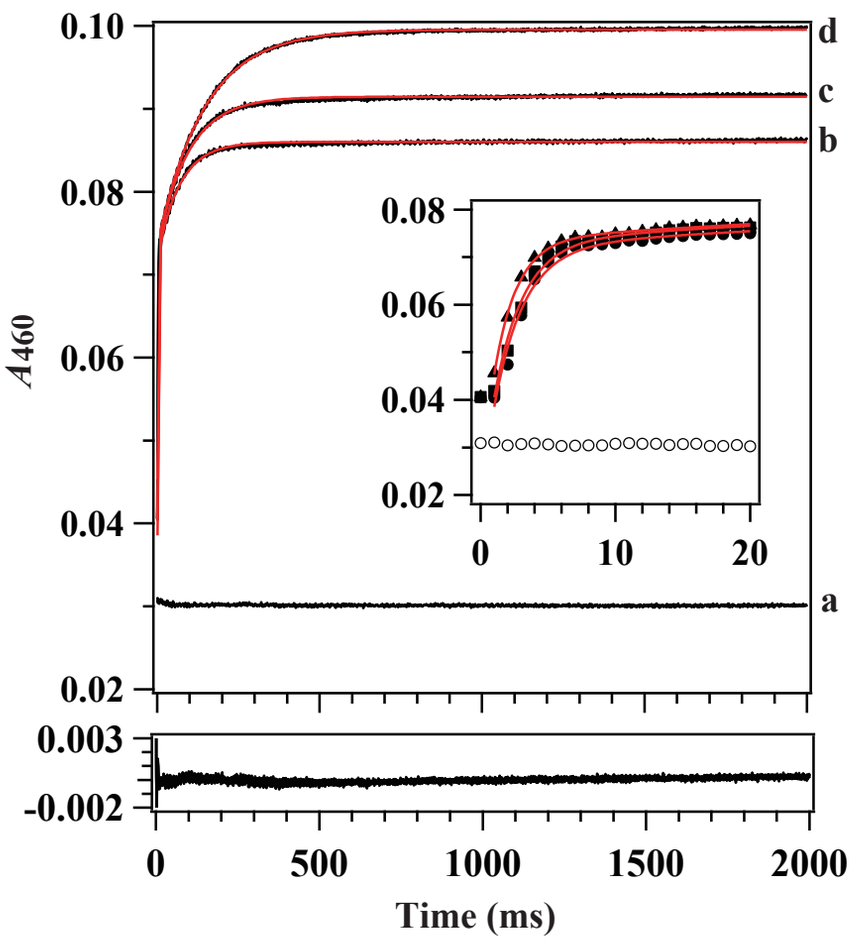
0.10
0.08
0.06
0.04
0.02
A460
d
c
b
a
0.08
0.06
0.04
0.02
0
10
20
0.003
-0.002
0
500
1000
1500
2000
Time (ms)

Figure 3A

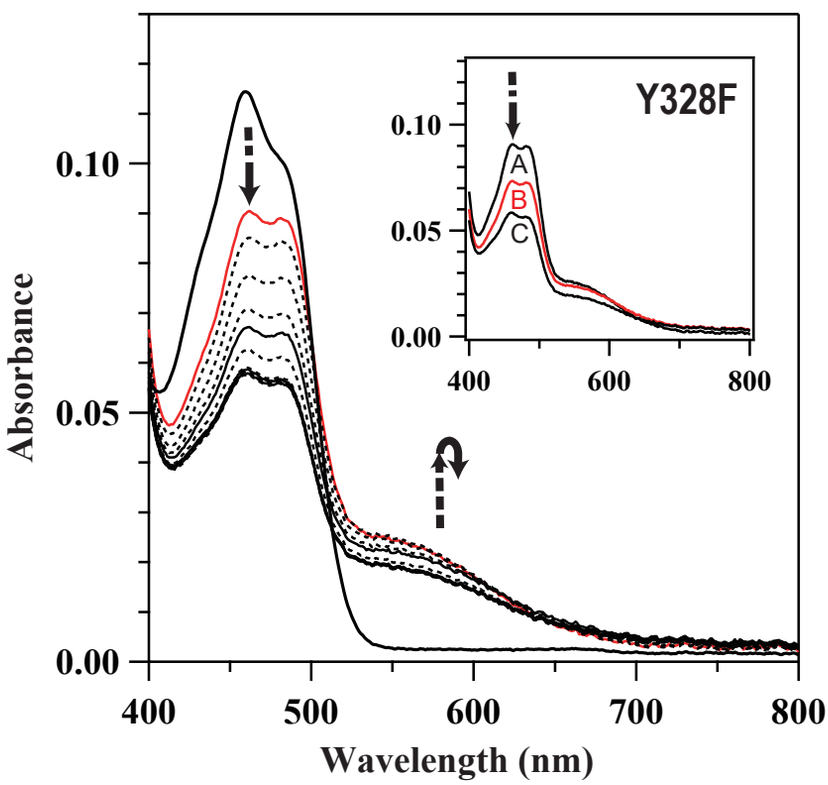
Absorbance
0.10
0.05
0.00
400
500
600
700
800
Wavelength (nm)
Y328F
A
B
C

Figure 3b

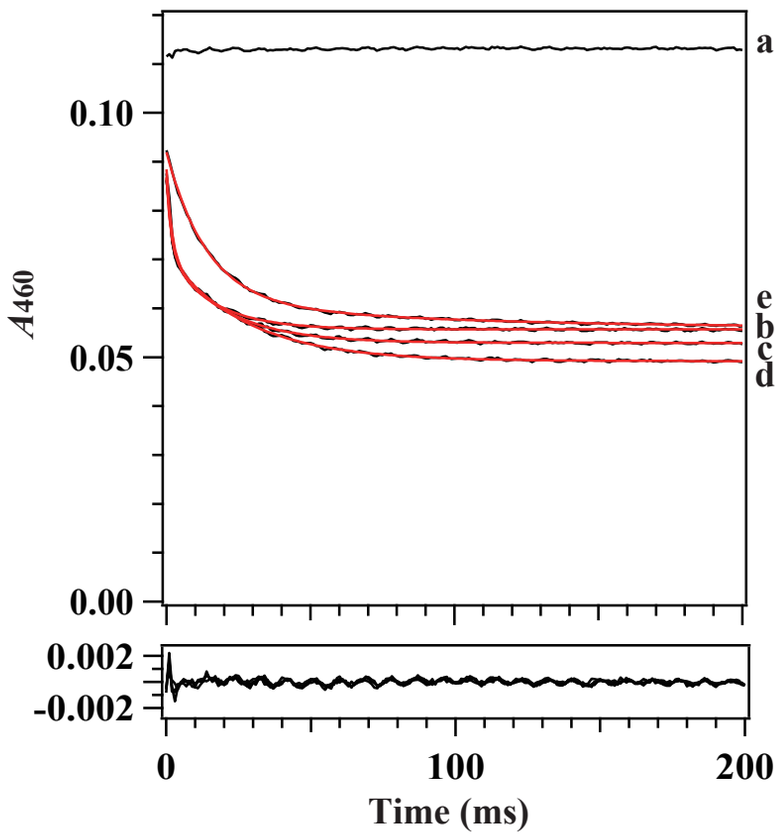

Figure 3C

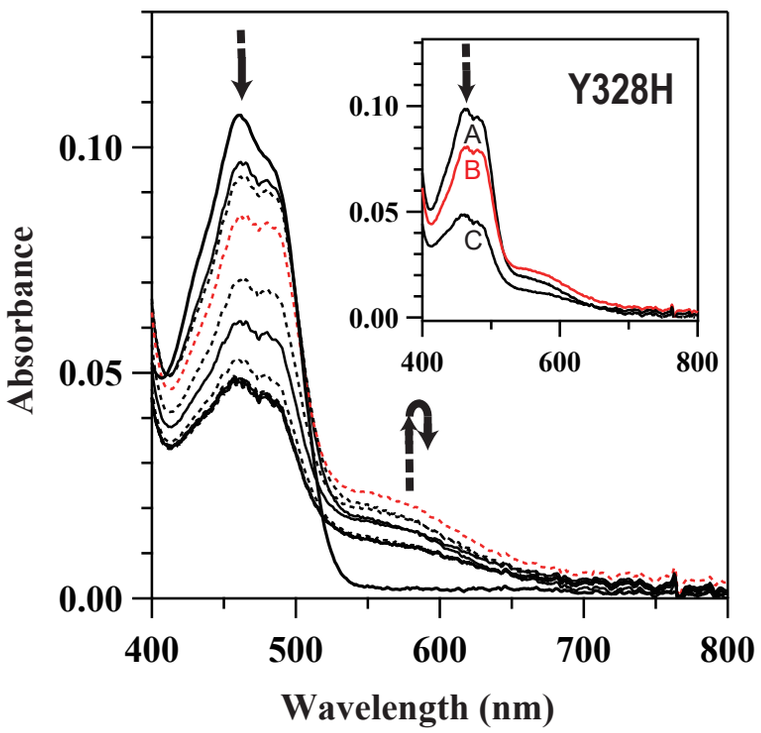
Absorbance
0.10
0.05
0.00
400
500
600
700
800
Wavelength (nm)
Y328H
A
B
C
0.10
0.05
0.00
400
600
800

Figure 3d

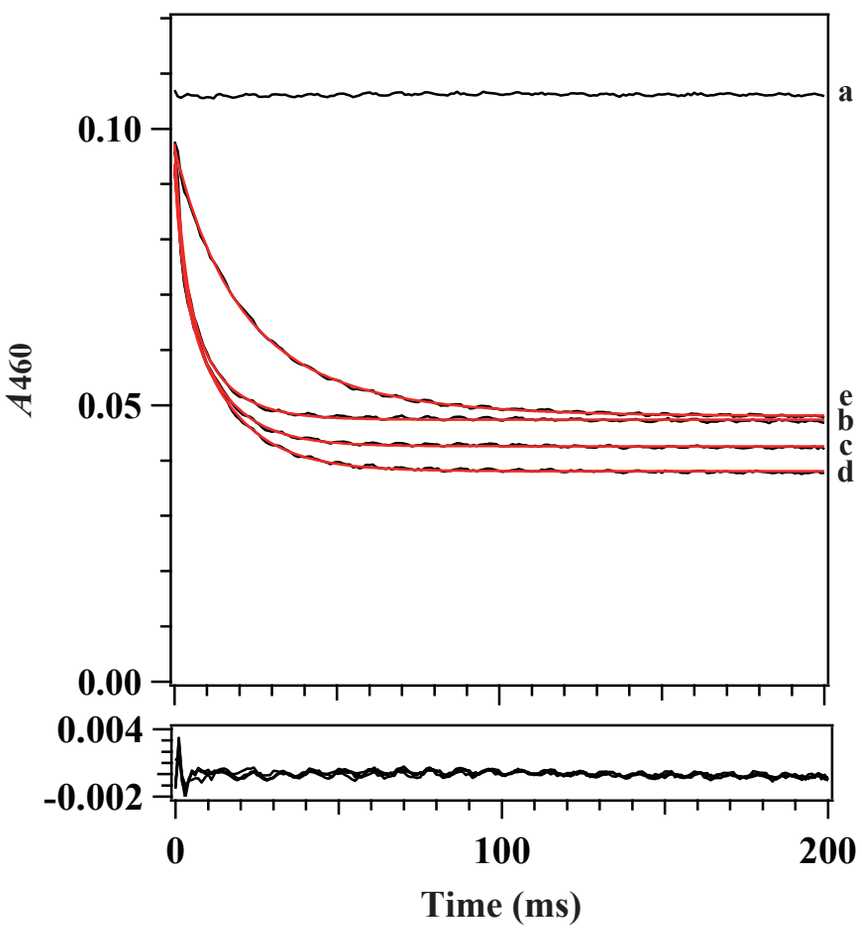

Figure 3E

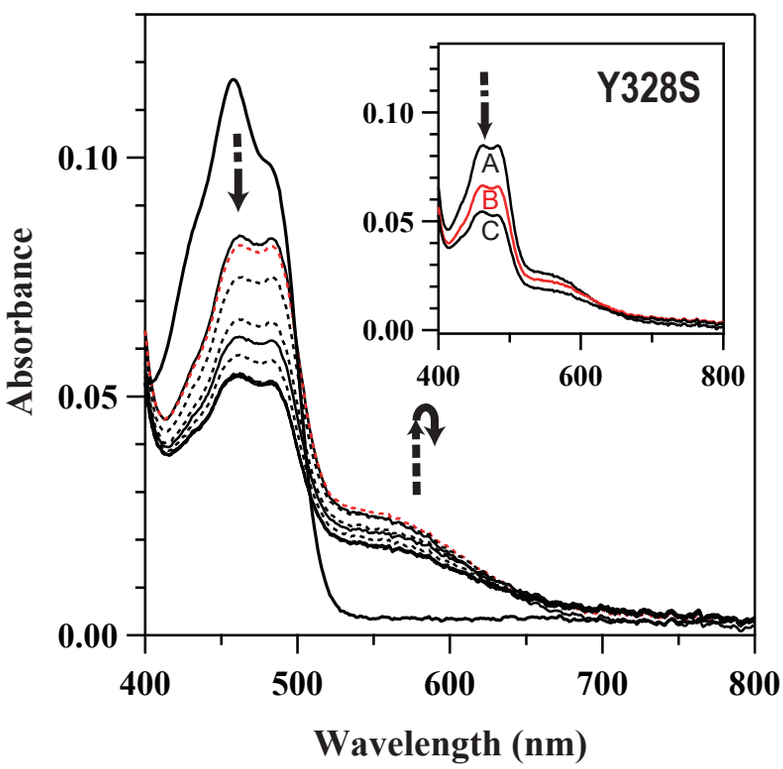
Y328S
A
B
C
0.10
0.05
0.00
400
600
800
Absorbance
0.10
0.05
0.00
400
500
600
700
800
Wavelength (nm)

Figure 3f

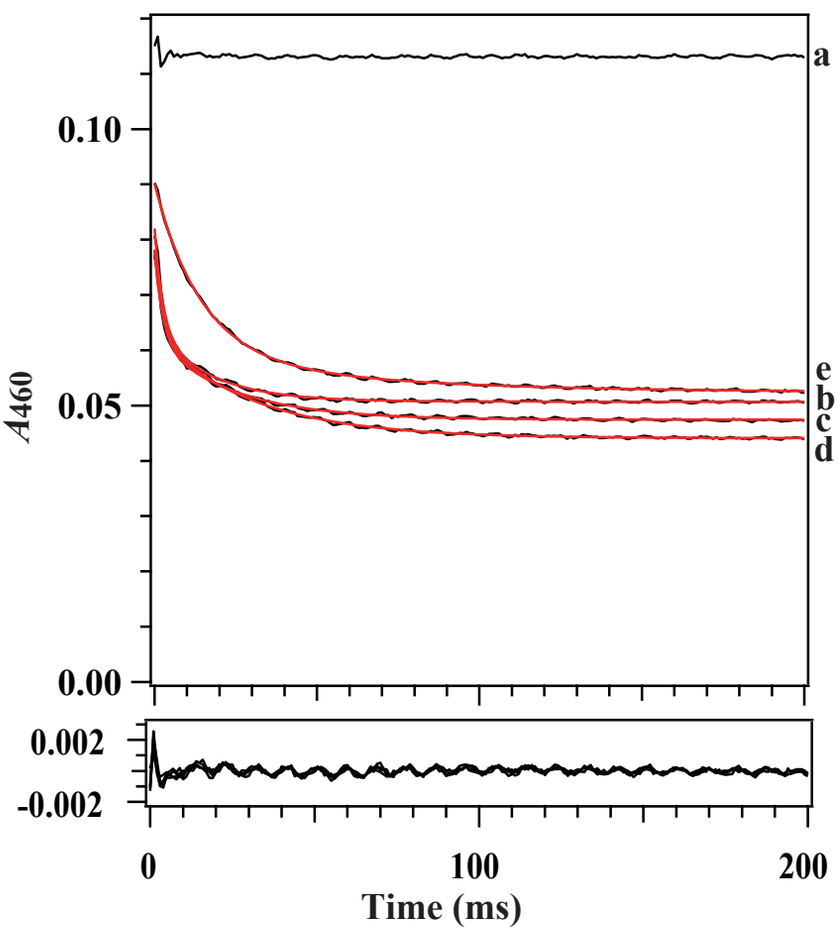

Figure 4A

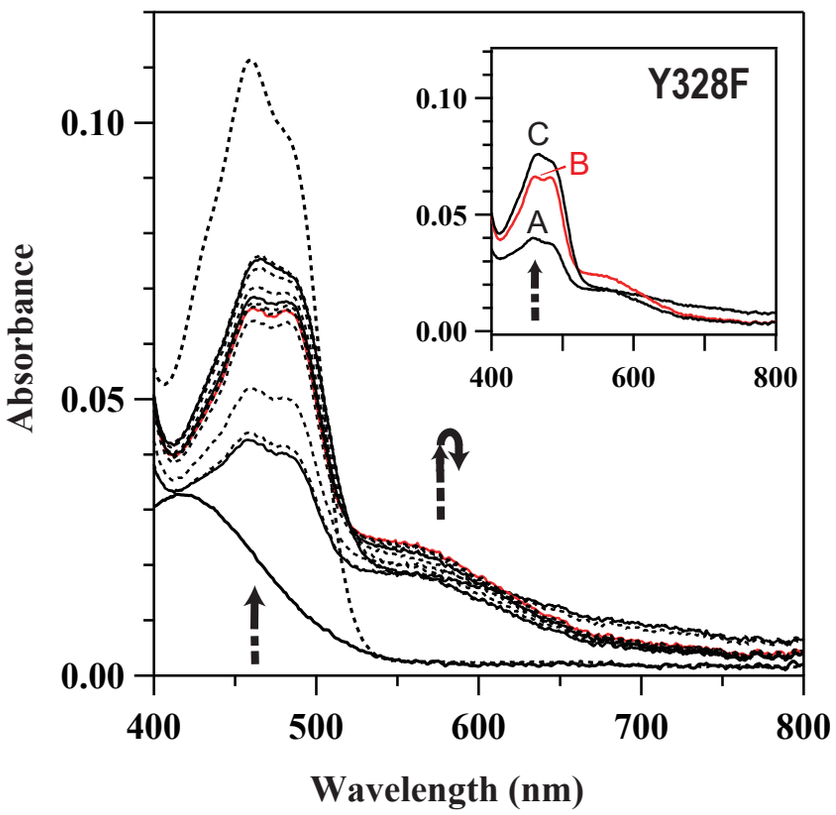
Absorbance
0.10
0.05
0.00
400
500
600
700
800
Wavelength (nm)
Y328F
C
B
A
0.10
0.05
0.00
400
600
800

Figure 4b

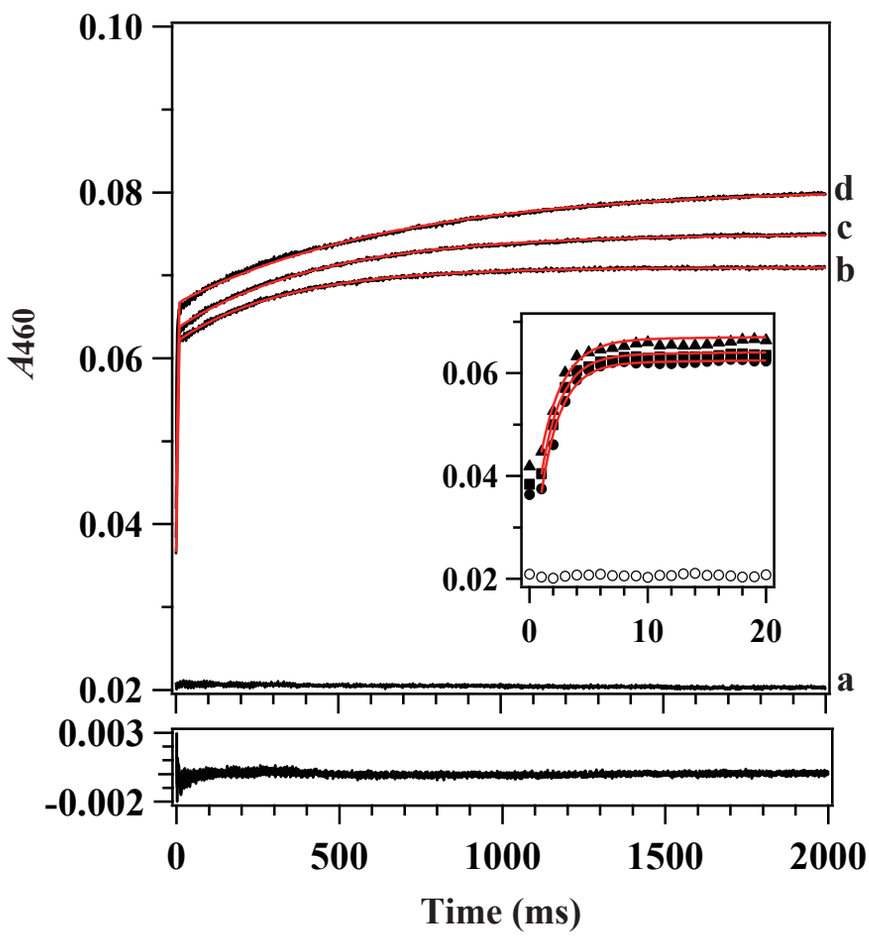
0.10
0.08
0.06
0.04
0.02
A460
d
c
b
a
0.06
0.04
0.02
0
10
20
0.003
-0.002
0
500
1000
1500
2000
Time (ms)

Figure 4C

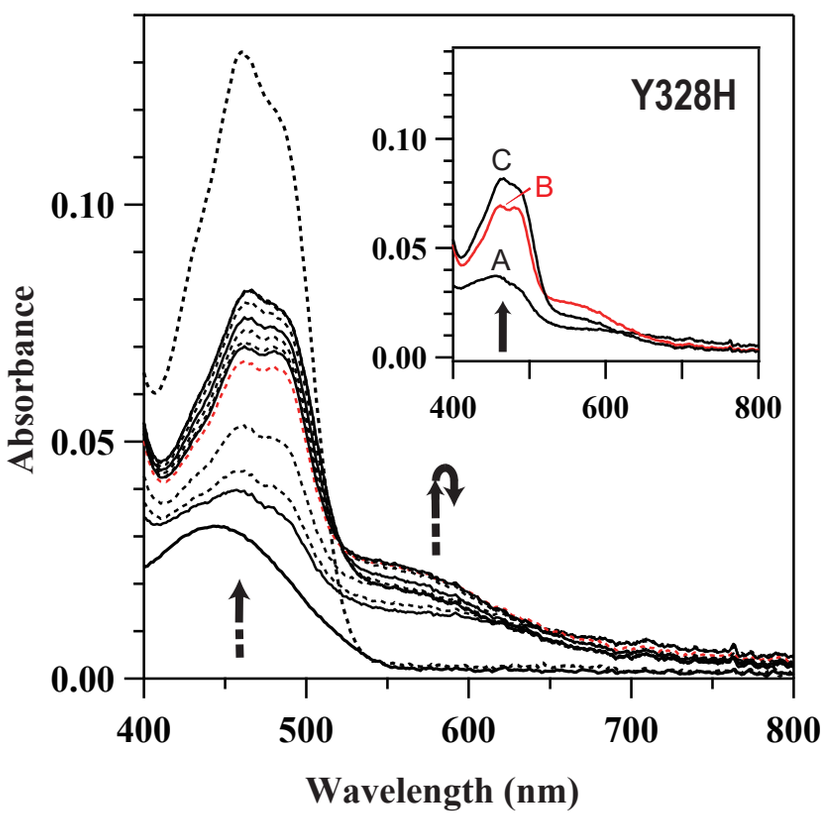
Y328H
C
B
A
0.10
0.05
0.00
400
600
800
Absorbance
0.10
0.05
0.00
400
500
600
700
800
Wavelength (nm)

Figure 4d

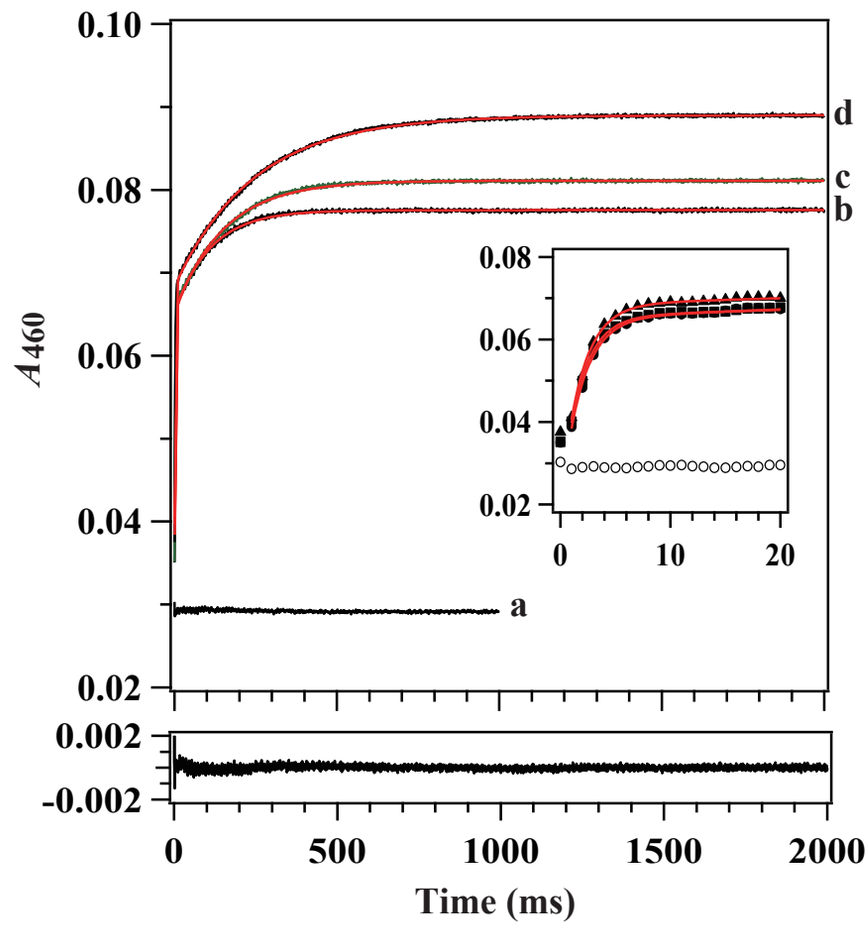
0.10
0.08
0.06
0.04
0.02
A460
d
c
b
a
0.08
0.06
0.04
0.02
0
10
20
0.002
-0.002
0
500
1000
1500
2000
Time (ms)

Figure 4E

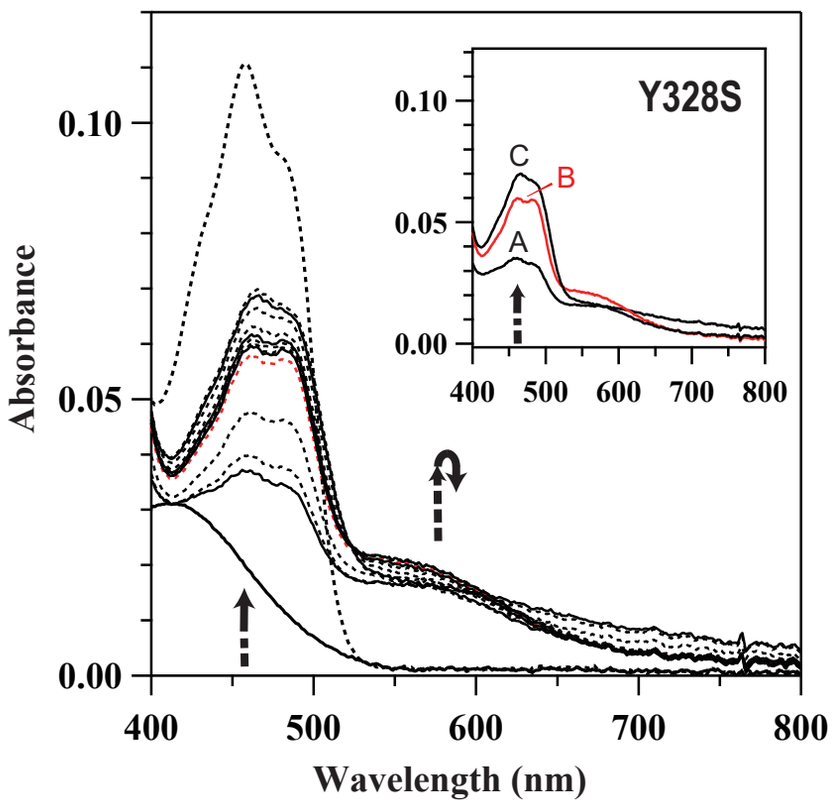
Absorbance
0.10
0.05
0.00
400
500
600
700
800
Wavelength (nm)
Y328S
C
B
A
0.10
0.05
0.00
400
500
600
700
800

Figure 4f

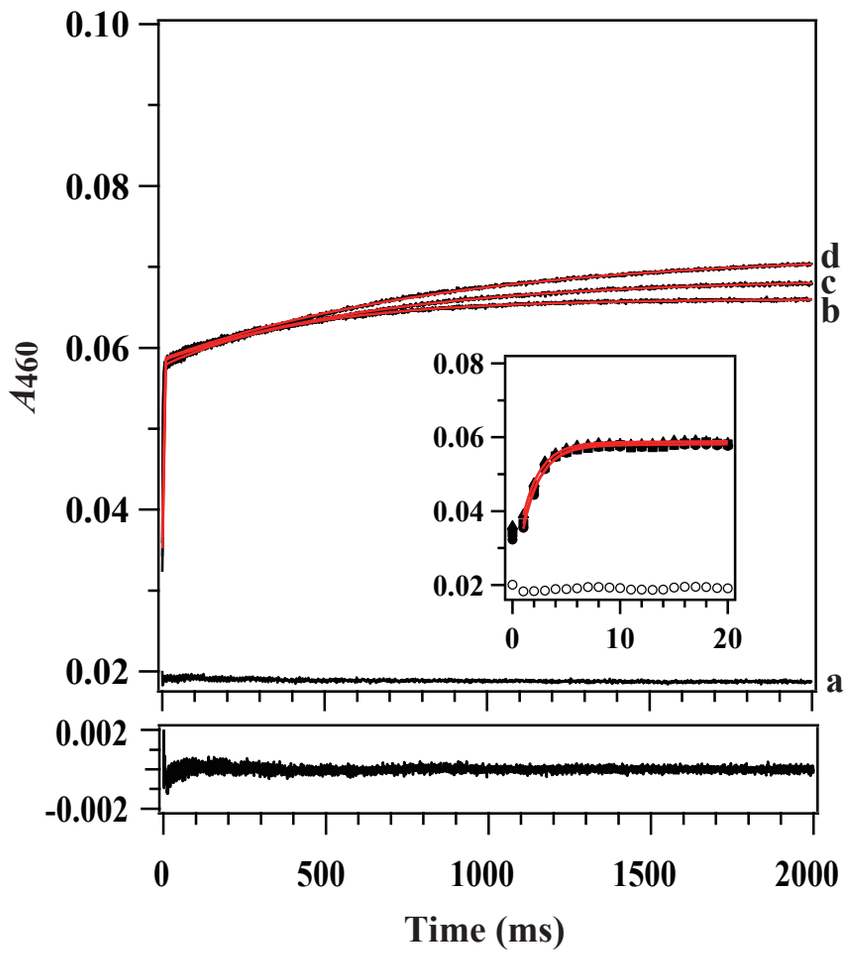
0.10
0.08
0.06
0.04
0.02
A460
d
c
b
a
0.08
0.06
0.04
0.02
0
10
20
0.002
-0.002
0
500
1000
1500
2000
Time (ms)

Figure 5A

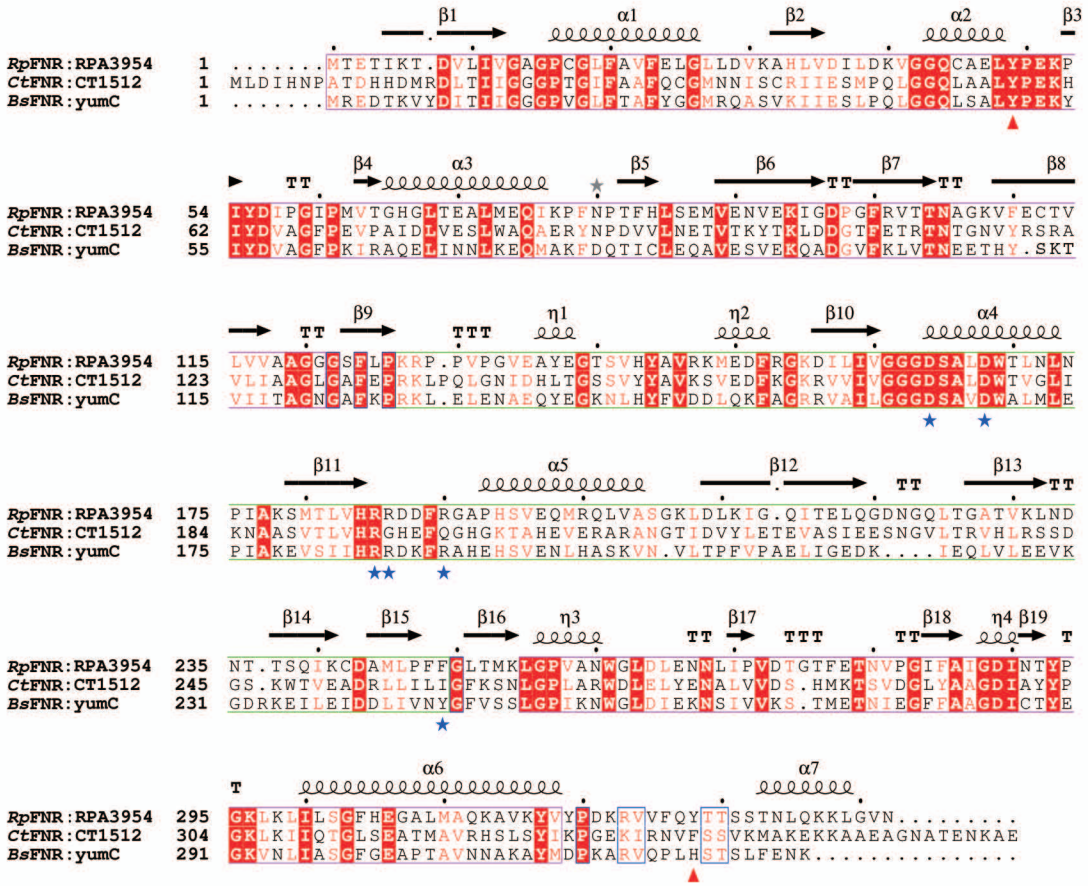

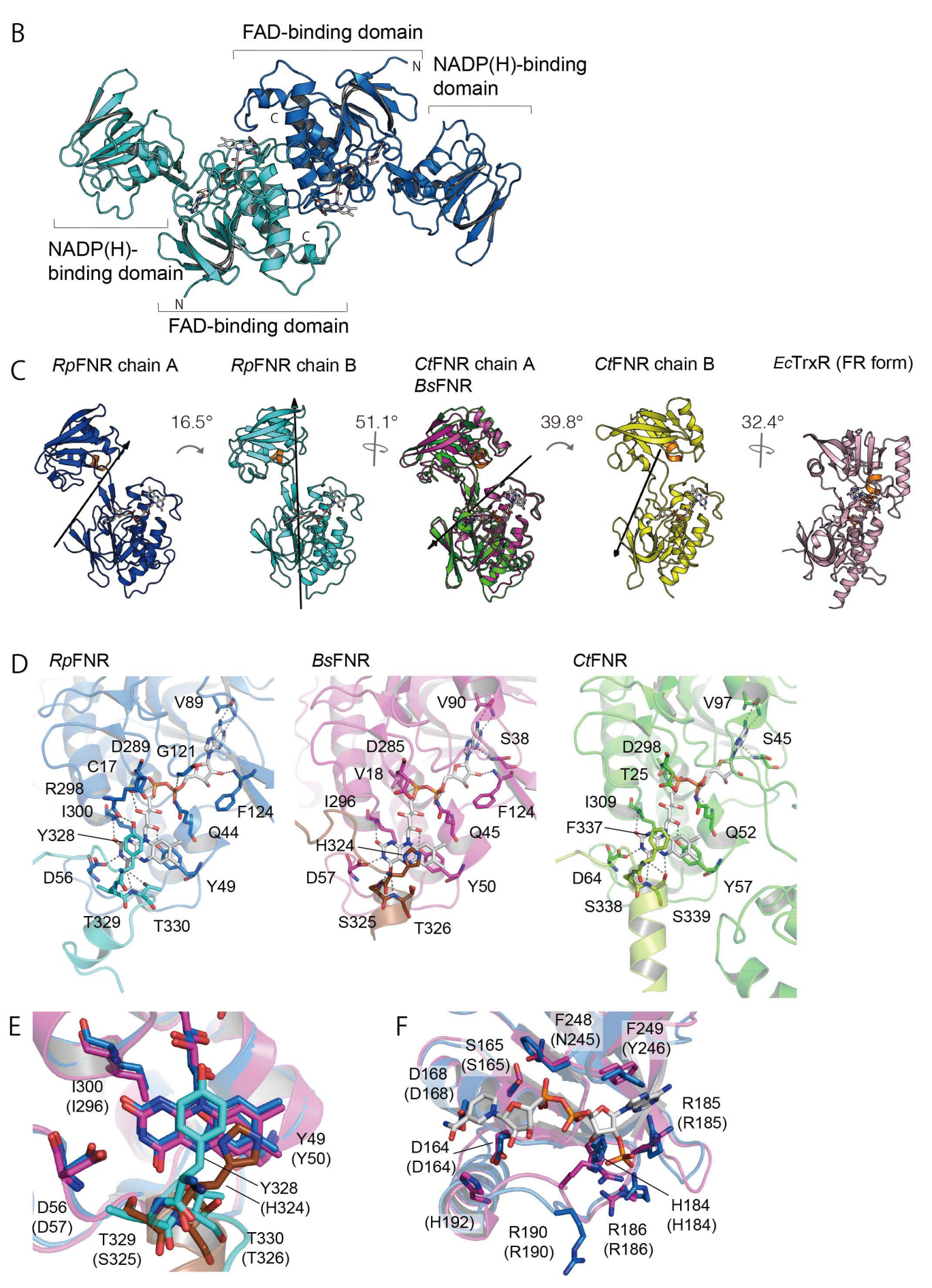
B
FAD-binding domain
N
NADP(H)-binding domain
C
C
NADP(H)-binding domain
N
FAD-binding domain
C
RpFNR chain A
RpFNR chain B
CtFNR chain A
BsFNR
CtFNR chain B
EcTrxR (FR form)
16.5°
51.1°
39.8°
32.4°
D
RpFNR
V89
D289
G121
C17
R298
I300
F124
Y328
Q44
D56
Y49
T329
T330
BsFNR
V90
S38
D285
V18
I296
F124
Q45
H324
D57
Y50
S325
T326
CtFNR
V97
S45
D298
T25
I309
F337
Q52
D64
Y57
S338
S339
E
I300
(I296)
Y49
(Y50)
Y328
(H324)
D56
(D57)
T329
(S325)
T330
(T326)
F
F248
(N245)
F249
(Y246)
S165
(S165)
D168
(D168)
R185
(R185)
D164
(D164)
H184
(H184)
(H192)
R190
(R190)
R186
(R186)

Figure S1

SDS-PAGE analysis of the wild type and mutated *Rp*FNR proteins with Coomassie Brilliant Blue staining. Lanes 1 to 5 were loaded with molecular weight markers (250, 150, 100, 75, 50, 37, 25, 20, 15 and 10 kDa from the top), WT, Y328F, Y328H and Y328S *Rp*FNRs, respectively (approximately 50 pmol / lane).

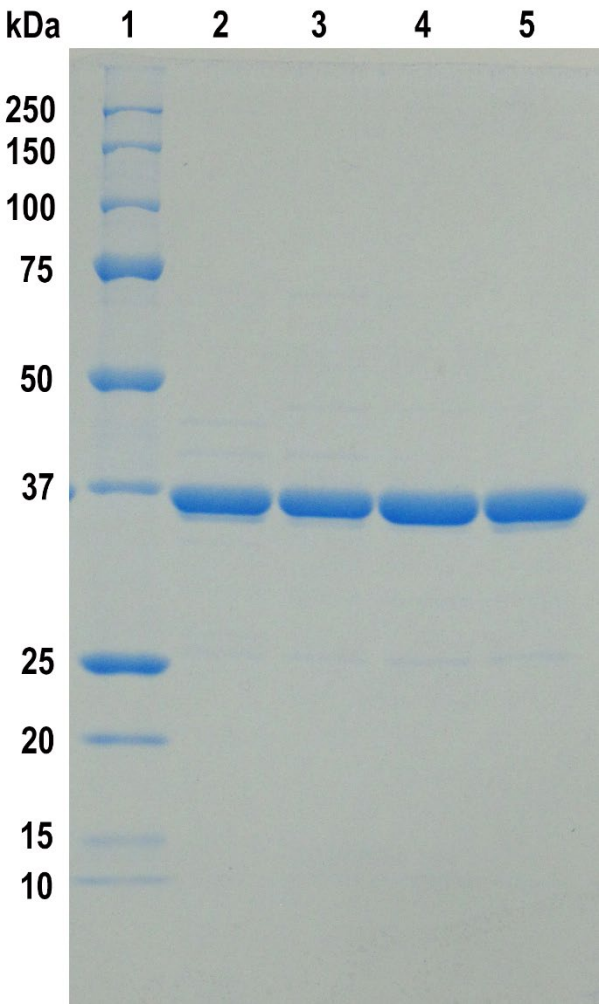

Figure S2

(a) Time course of A_{590} after mixing wild type *Rp*FNR$_{ox}$ with NADPH or S-NADPD. The measurement conditions were the same as those in Fig. 2a at the NADPH concentrations of 0 µM (trace a), 100 µM (trace b), 200 µM (trace c), 500 µM (trace d) or 100 µM S-NADPD (trace e, red line). The data are an average of five measurements. (b) Transient spectra induced by mixing 9.4 µM wild type *Rp*FNR$_{ox}$ with 100 µM *S*-NADPD. The reaction was performed in 20 mM HEPES-NaOH buffer (pH 7.0) at 10°C. The spectra at 0, 10, 100 and 1000 ms are shown as thin continuous lines, and those at 1, 2, 5, 20, 50, 200 and 500 ms are shown by thin dotted lines from the top to the bottom at 450 nm, respectively. The spectrum of oxidized wild type *Rp*FNR is shown as a thick continuous line. The arrows indicate the directions of the absorbance changes at the respective wavelengths. The dashed parts of the arrows indicate that absorption change occurred within the first data acquisition period (~1 ms). The inset shows the spectrum of each kinetic component resulting from global analysis with two step sequential reaction model (A →B→C [fast/slow]). (c) The time course of A_{590} after mixing wild type *Rp*FNR$_{red}$ with NADP$^+$. The measurement conditions were the same as those in Fig. 2d with the NADP$^+$ concentrations of 0 µM (trace a), 100 µM (trace b), 200 µM (trace c) or 500 µM (trace d). The data are an average of four to five measurements.

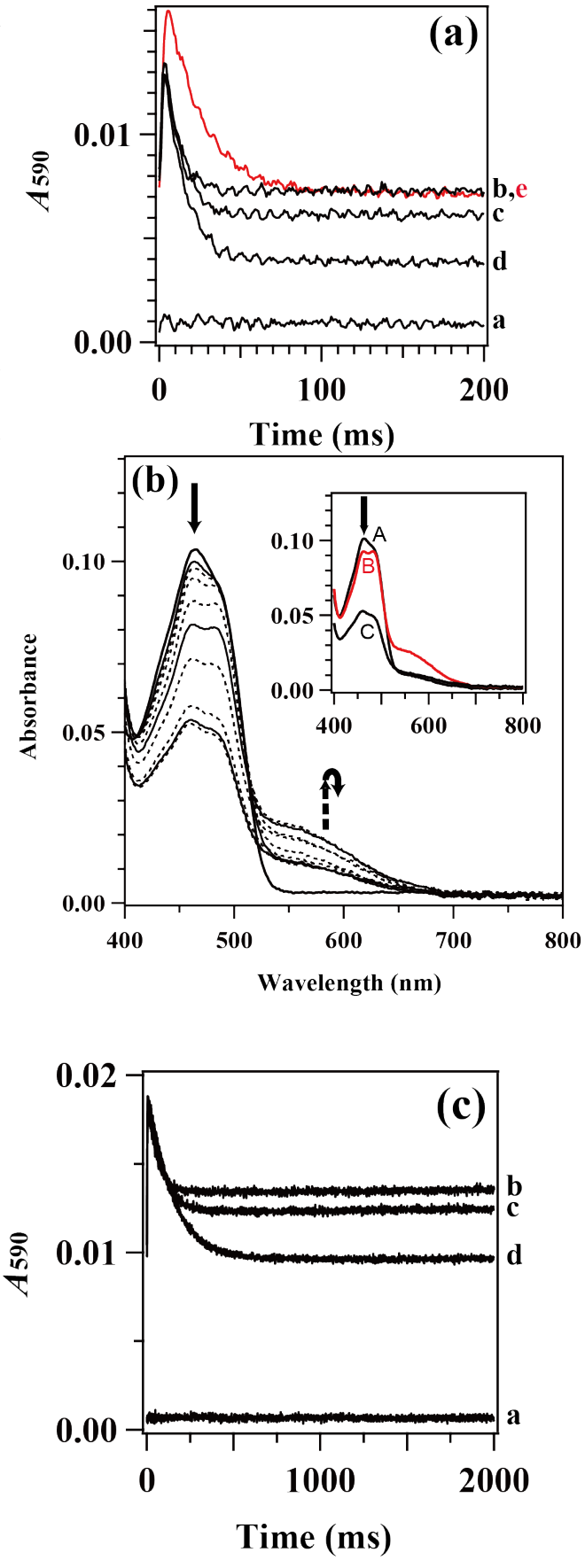

Figure S3

The time course of A_{590} after mixing oxidized (a) Y328F, (b) Y328H and (c) Y328S *Rp*FNRs with NADPH and *S*-NADPD. The measurement conditions were the same as those in Fig. 3b, d, f. An average of five measurements at NADPH concentrations of 0 μM (trace a), 100 μM (trace b), 200 μM (trace c) and 500 μM (trace d), and 100 μM *S*-NADPD (trace e, red line) are indicated

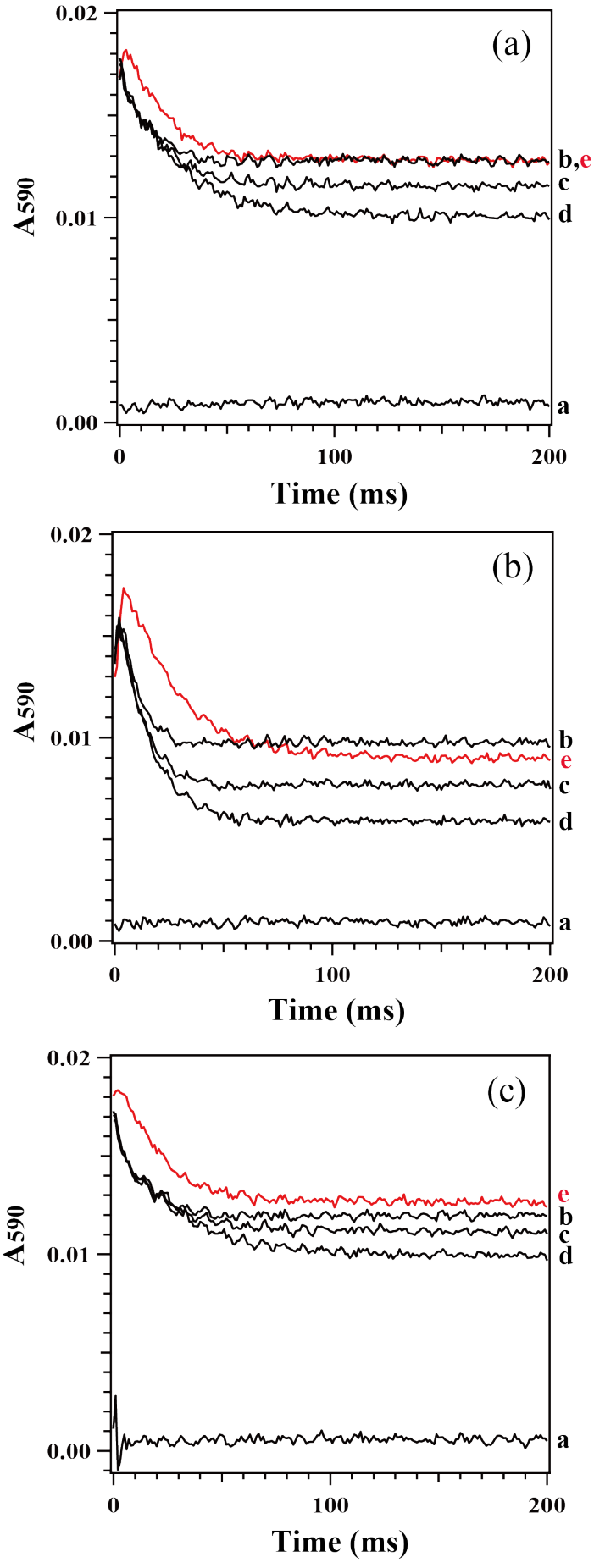

Figure S4

The time course of A_{590} after mixing reduced (a) Y328F, (b) Y328H and (c) Y328S *Rp*FNRs with $NADP^+$. The measurement conditions were the same as those in Fig. 4b, d, f. The data of an average of five measurements at $NADP^+$ concentrations of 0 μM (black), 100 μM (red), 200 μM (blue) or 500 μM (green) are indicated.